UNIVERSIDADE DE LISBOA
FACULDADE DE CIÊNCIAS
DEPARTAMENTO DE FÍSICA

Monte Carlo Simulations of Ionization Chamber Perturbation Factors in Proton Beams

Daniela Botnariuc

Mestrado Integrado em Engenharia Biomédica e Biofísica
Perfil em Radiações em Diagnóstico e Terapia

Dissertação orientada por:

Prof. Dr. Luís Peralta
Dr. Ana Mónica Lourenço

2019

ACKNOWLEDGEMENTS

First, I would like to thank Prof Gary Royle for giving me the opportunity to become part of the amazing proton therapy groups at University College London (UCL) and the National Physical Laboratory (NPL). I am specially grateful to my supervisor, Dr Ana Mónica Lourenço (UCL and NPL), who supported me everyday for a year and without whom this project would have not happened. To Ana Mónica, a huge thank you for being available whenever I had any questions, for the long discussions about protons, electrons and stopping powers, for her priceless guidance, help and friendship. I would also like to express my gratitude to Prof Luís Peralta, Faculty of Sciences of the University of Lisbon (FCUL), for his patience during poor quality Skype calls, for all his suggestions and advice. A sincere thank you for everything I have learned from him during the past years in the classroom and lab but, most importantly, for passing on the passion for radiation and dosimetry.

I would like to acknowledge everyone in the Medical Radiation groups at NPL. To David Shipley, for helping me to solve my recurring IT problems and to Hugo Palmans, for discussing Monte Carlo and dosimetry problems related to my simulations. To Russell Thomas, for his cheerful mood. I couldn't be more grateful for the opportunities given to me during my stay at NPL. I have had the chance to participate in the 5^{th} edition of Proton Physics Research and Implementation Group (PPRIG) workshop. I am also thankful for the unique opportunity to take part in experiments at Paul Scherrer Institut (PSI), in Switzerland and at The Christie NHS Foundation Trust - a high-energy proton beam facility in the UK.

An acknowledgement is addressed to Erasmus for making this internship easier from a financial point of view. I would also like to acknowledge the use of the UCL Myriad High Throughput Computing Facility (Myriad@UCL) and the UCL Legion High Performance Computing Facility (Legion@UCL), and associated support services, in the completion of this work. A genuine thank you to the FLUKA mailing list for answering to all my questions about the code.

I am really grateful for the people I have met in London and made this internship an amazing time of my life. A huge thank you to the Succulent Squad, for offering me a dead succulent and sharing the hall with me everyday. To Hannah, for always having a good story to tell and for cheering me up every time I needed. To Reem and Charles, for inspiring me with awesome science. A kind and special thank you to Michael, for correcting all the commas in this dissertation and for always being there for me. A big thank you to my fittest friends in the world, Inês and Beatriz, for always being online for me and to Bruna, for her longtime friendship.

A loving thank you to my family, especially my mum and dad, for the continuous support, love and encouragement throughout my life. To my brother and Nicole, for not forgetting to send me photos and videos of my nephew. Thank you all for always believing in me.

ABSTRACT

Currently, user reference instruments used in proton dosimetry (proton beam quality, Q) are calibrated at Primary Standard Dosimetry Laboratories (PSDL) in Cobalt-60 beams (beam quality Q_0). The difference in the beam qualities is taken into account in the calculation of absorbed dose to water, $D_{water,Q}$, by introducing the beam quality correction factor, k_{Q,Q_0}. In the analytical calculation of k_{Q,Q_0}, all available protocols for reference dosimetry in proton therapy assume ionization chamber perturbation factors, p_Q, which account for the non-water equivalence of the air cavity and entrance window of these detectors, to be unity. This amounts to an uncertainty in the determination of $D_{water,Q}$ of 4.6%. This project aimed to determine accurately ionization chamber perturbation factors for the PTW-34070 Bragg Peak® chamber in narrow mono-energetic proton beams of 60 MeV, 150 MeV and 250 MeV, and for the PTW-34001 Roos® chamber in a spread-out Bragg peak, using FLUKA Monte Carlo code. The influence of different secondary charged particles on p_Q was studied, especially that of secondary electrons, which has not been studied before.

The computation of ionization chambers response is sensitive to boundary crossing artifacts, as particles travel between multiple regions with varying densities. Transport algorithms were validated in FLUKA by performing a Fano cavity test for a plane-parallel ionization chamber, for low-energy protons. FLUKA passed the Fano test within 0.1% accuracy.

Ionization chamber perturbation factors were calculated by simulating different geometries of the two chambers, using the same transport parameters that were validated in the Fano test. For the PTW-34070 Bragg Peak® chamber the perturbation introduced by the air cavity was close to unity for all proton initial energies. Contrary, the presence of the chamber's wall resulted in perturbations in dose up to 1%. Overall, p_Q differed from unity by approximately 1%. The simulation of ionization chamber perturbation factors in the modulated beam showed to be extremely time consuming thus, it was not possible to obtain significant results with the available resources.

Ionization chamber perturbation factors can amount to a correction of 1% in high-energy mono-energetic beams, when all secondary charged particles were transported. These factors must be calculated for all ionization chambers used in proton dosimetry and accounted in the calculation of the k_{Q,Q_0}. Further investigations must consider the calculation of ionization chamber perturbation factors in modulated beams.

Key words: Proton therapy, dosimetry, ionization chamber perturbation factors, Fano cavity test, Monte Carlo.

RESUMO

A maior motivação em radioterapia para o tratamento de cancro passa por diminuir a dose administrada a tecidos saudáveis, mantendo ou aumentando a dose depositada no tumor. Ao longo dos anos, inúmeros avanços tecnológicos permitiram ir ao encontro desse objetivo, tais como: a computarização e automatização dos sistemas de planeamento do tratatmento, o desenvolvimento de técnicas de imagem avançadas que permitem uma localização rigorosa do tumor, assim como a introdução de novos tipos de radiação com características de deposição de dose mais favoráveis em comparação com aquela obtida tradicionalmente com radiação-X. O uso de protões em radioterapia apresenta a vantagem destas partículas pararem totalmente nos tecidos, protegendo assim os órgãos a seguir ao alvo de irradiação. Ao atravessarem um meio, taxa de perda de energia dos protões aumenta à medida que estes ficam menos energéticos, depositando um máximo de energia, designada a região do pico de Bragg, antes de perderam toda a sua energia, pararando completamente. O alcance dos protões pode ser manipulado através da modulação da sua energia inicial de modo a que o pico de Bragg coincida com a região do tumor. Clinicamente, a combinação de feixes de energias diferentes produz uma região de dose uniforme em profundidade, designada por *spread-out Bragg peak* (SOBP).

Independentemente do tipo de radiação, a dose deve ser fornecida ao volume alvo com uma incerteza na ordem dos 5%, no intervalo de confiança de 95%. Esta incerteza deve ser entendida como a incerteza global que inclui todas as fontes de incerteza possíveis, como as que advêm do posicionamento do paciente, do planeamento do tratamento, da entrega de radiação, de procedimentos de calibração dos instrumentos utilizados, etc. No geral, para ter um máximo de 5% de incerteza global, a incerteza dosimétrica deve contribuir com aproximadamente 1%. Todas as unidades de radioterapia devem assegurar que aos pacientes são administradas doses com níveis de incerteza internacionalmente aceites. De forma a obter uniformidade no campo da dosimetria, todos os instrumentos de referência de medição da dose devem ser rastreáveis a Laboratórios de Dosimetria de Padrões Primários (PSDL).

Este projeto foi desenvolvido na área da dosimetria de protões e teve lugar na University College London (UCL) e no Laboratório de Dosimetria de Padrões Primários - o Laboratório Nacional de Física (NPL) - no Reino Unido. Em dosimetria, a grandeza de interesse é a dose absorvida em água. Atualmente, os PSDL não possuem feixes de protões (qualidade de feixe Q) nas suas instalações. Por esta razão, a calibração dos intrumentos de referência dos centros de protões, geralmente câmaras de ionização, é feita em feixes de Cobalto-60 (qualidade de feixe de referência Q_0). Devido ao facto da calibração das câmara de ionização de referência ser feita numa qualidade de feixe diferente daquela na qual os detetores operam, é necessário introduzir um factor extra, k_{Q,Q_0}, no cálculo da dose absorvida em água, $D_{\mathrm{water},Q}$. Este fator, conhecido como o factor de correção da qualidade de feixe, é calculado analiticamente e introduz uma incerteza de 4.2% na determinação da dose absorvida em água. Esta é, de facto, a principal contribuição para a incerteza de $D_{\mathrm{water},Q}$ nos feixes de protões, que por sua vez é da ordem dos 4.6%, enquanto que uma incerteza de apenas 1.5% é aplicada em feixes de fotões. De modo a tirar maior partido do potencial que a terapia com protões apresenta, é necessário diminuir as incertezas envolvidas na dosimetria de feixes de protões.

Um dos fatores envolvidos no cálculo de k_{Q,Q_0} é o fator de correção da perturbação das câmaras de ionização, p_Q, que corrige a perturbação que a cavidade de ar, p_{cav}, e a parede, p_{wall}, do detetor introduzem na fluência das partículas do feixe, por não serem constituídos por materiais equivalentes à água. O fator p_Q é então o produto de p_{cav} por p_{wall}. Nos protocolos de dosimetria de referência atualmente aplicados, p_Q são aproximados à unidade para todos os modelos de câmaras de ionização, mesmo que haja evidências que estes fatores apresentam uma correção de 1% em feixes de protões de alta energia. Um dos objetivos deste trabalho foi calcular os fatores de perturbação para a câmara de ionização PTW-34070 Bragg peak® em feixes mono-energéticos e mono-direcionais de 60 MeV, 150 MeV e 250 MeV. Os fatores p_Q foram também calculados para o detetor PTW-34001 Roos® num feixe modulado. Os fatores de perturbação foram obtidos através de simulações realizadas no código de Monte Carlo (MC) FLUKA. Ambos os detetores foram modelados no FLUKA de acordo com as especificações do fabricante. Contrariamente aos estudos feitos anteriormente nesta área, o presente trabalho considerou o transporte de todas as partículas secundárias do feixe, incluindo partículas pesadas carregadas e eletrões.

A computação da resposta de câmaras de ionização é sensível a artefactos que possam surgir quando as partículas atravessam múltiplas regiões de densidades distintas. De facto, estas são transportadas da região que corresponde à parede da câmara de ionização, que tem uma densidade semelhante à da grafite, para uma cavidade de ar, que tem uma densidade mil vezes inferior. De modo a evitar artefactos nas simulações, os parâmetros de transporte das partículas no FLUKA tais como a energia perdida num passo de história condensada (CH), o cálculo das secções eficazes, o tamanho do passo, devem ser otimizados através de um teste de auto-consistência (teste de Fano), que é suportado pelo teorema de Fano. Este teorema afirma que, em condições de equilíbrio de partículas carregadas (CPE), a fluência das partículas carregadas é independente de variações de densidade de ponto em ponto, considerando que as secções eficazes são uniformes em todo o fantoma simulado. Uma forma de implementar este teorema é simular uma distribuição uniforme de partículas por unidade de massa num fantoma cujas regiões tenham a mesma composição molecular mas densidades diferentes. O código de MC passará o teste se a dose nas diferentes regiões do fantoma for uniforme.

O teste de Fano foi realizado para otimizar o transporte de partículas no FLUKA num feixe de protões a baixas energias (20 MeV), para a câmara de ionização PTW-34001 Roos®. Para implementar o teste de Fano, a câmara de ionização foi simulada num fantoma de água em que a todas as regiões do detetor foi atribuído o mesmo material, neste caso água, de forma a que as propriedades atómicas sejam uniformes em toda a geometria, mantendo as suas densidades originais. A fonte homogénea de protões foi obtida no FLUKA através de uma rotina modificada do ficheiro "source.f" em que o número de partículas geradas em cada região do fantoma é inversamente proporcional à densidade da região. A dose foi calculada em todas as regiões do fantoma. A diferença relativa nas doses calculadas nas diferentes regiões foi de 0.05%. O FLUKA passou o teste de Fano com uma exatidão de 0.1%.

Os fatores de perturbação para a PTW-34070 Bragg peak® e PTW-34001 Roos® foram calculados através do cálculo da dose em diferentes geometrias simplificadas das câmaras de ionização. Sendo a quantidade de interesse a dose absorvida em água, a dose foi primeiramente calculada numa gometria que consistia numa fina camada de água com um raio igual ao da cavidade de ar da câmara de ionização. Seguidamente, a dose foi calculada na cavidade de ar das respetivas câmaras de ionização considerando que o revestimento da cavidade de ar é composto pelo material do fantoma - que neste caso foi água. Através do cálculo da dose na cavidade de água e na cavidade de ar, é possível inferir sobre a perturbação introduzida pela presença das cavidades de ar, p_{cav}, dos dois detetores. Finalmente, a última geometria simulada consistiu no modelo original das câmaras de ionização, no qual todos os materiais que compõem as câmaras de ionização foram considerados. Comparando a dose na cavidade de ar quando toda a geometria dos detetores é considerada e a dose na geometria que continha apenas a cavidade de ar é possível obter a perturbação causada pela presença do revestimento da cavidade de ar, p_{wall}, dos detetores. Para a câmara de ionização PTW-34070 Bragg peak®, p_{cav} foi próximo da unidade para todas as energias dos feixe mono-energéticos e mono-direcionais coniderados. Quanto a p_{wall}, este constituiu uma correção de 1% para feixes de protões de 250 MeV. De forma geral, quando todas as partículas secundárias foram transportadas, p_Q contribuiu com uma correção até 1% no cálculo da dose absorvida em água. As simulações dos fatores de perturbação no SOBP mostraram ser extremamente demoradas do ponto de vista computacional, de modo que não foram obtidos resultados significativos.

De forma a diminuir a incerteza nos k_{Q,Q_0}, os fatores de perturbação das câmaras de ionização, p, devem ser calculados considerando o espectro completo das partículas secundárias em feixes de protões.

Palavras-chave: Terapia de protões, dosimetria, fatores de perturbação das câmaras de ionização, teste de Fano, Monte Carlo.

CONTENTS

LIST OF FIGURES

LIST OF TABLES

LIST OF ABBREVIATIONS

BG Bragg-Gray

CH Condensed History

CPE Charged particle equilibrium

MC Monte Carlo

NPL National Physical Laboratory

PSDL Primary Standards Dosimetry Laboratory

RNG Random Number Generator

SSDL Secondary Standards Dosimetry Laboratory

SA Spencer-Attix

SOBP Sprea-out Bragg peak

WET Water-equivalent thickness

1 INTRODUCTION

1.1 RADIOTHERAPY

As reported by the World Health Organization, cancer is the second leading cause of death in the world and it was responsible for an estimated 9.6 million deaths in 2018 [4, 5]. In the initial stage of cancer development, the tumour is commonly confined to a specific anatomical tissue, in which it starts growing. While the disease is still well localized, surgical procedure or radiation therapy is the elected approach for treatment. In case the tumour is in close proximity to a vital organ or completely inaccessible with surgery, radiation therapy will be the preferred method. As the disease progresses, cancers can spread from their site of origin to nearby lymph nodes and start growing into other tissues or organs, evolving to metastases. To treat metastatic cancers, the suggested approaches are chemotherapy and immunotherapy, which are systemic methods. All cancer treatment techniques just described can be performed either as single treatments or, more commonly, in combination. This project will focus on radiation therapy for tumour eradication using protons.

In general, radiation can interact with biological tissue and cause direct or indirect damage to the genetic material (deoxyribonucleic acid, DNA). Direct damage occurs with the direct ionisation of the DNA strand by radiation whereas indirect damage occurs by ionising water molecules, which creates reactive free radicals that can provoke harmful intracellular reactions. Both damage types can lead to lethal reactions in the cell and the likelihood of cell death increases with increasing radiation dose. The major drawback in radiotherapy is that radiation affects both malignant cells and healthy tissues, thus, it is necessary to find the correct compromise between tumour eradication and healthy tissue damage [6].

Radiation killing of single cells is stochastic since it depends on the occurrence of individual ionizing events. However, if a tumour mass or organ is considered, the effect of radiation is deterministic, i.e. there is a dose threshold bellow which no clinical response will be observed and a dose above which the effect will be observed in every individual. This is illustrated in figure 1.1 where tumour control (solid line) and healthy tissue damage (dashed line) probabilities are presented as a function of dose. Tumours that can be treated with radiotherapy are those in which the tumour control curve appears on the left side of the healthy tissue damage curve. The more separated are these curves, the more effective will be the radiotherapy treatment. Note that both curves are very steep and consequently their dependence in dose is very high. For this reason, the uncertainty in dose delivered to patient should be as small as possible [7].

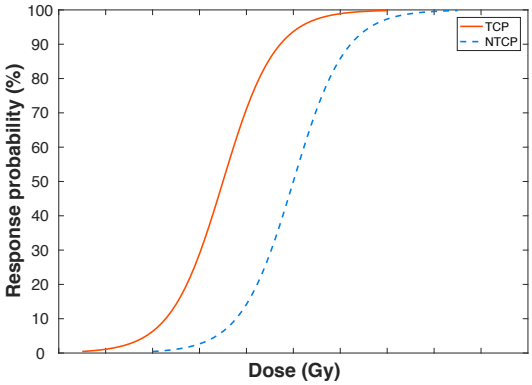

Figure 1.1: Tumour control probability (TCP) and normal tissue complication probability (NTCP) as a function of dose delivered to the patient.

The major goal and motivation for research in radiotherapy treatment techniques for cancer is to reduce delivered dose to healthy tissue while maintaining or increasing the dose to the target structure within acceptable uncertainty in order to improve patient outcomes. As recommended by the ICRU Report 24 [8], the absorbed dose to a target volume

in the patient should be delivered with an accuracy of 5% at 95% confidence level. This 5% includes different types of uncertainties, such as the uncertainty from calibration procedures in primary standard laboratories and reference absorbed dose measurements, as well as uncertainties introduced by patient positioning, treatment planning and dose delivery. For optimal treatment of patients, it is critical for dosimetric uncertainties to be as small as possible (around 1%).

1.2 ADVANTAGES OF PROTON THERAPY

Not long after the discovery of x-rays in 1895 [9], ionizing radiation was employed to treat cancer. Since then, research in physics and medicine has contributed to the improvement of radiation therapy and nowadays this is the main option for treatment in oncology [10]. Radiation interacts with matter via atomic and nuclear interactions. The mean energy deposited by the ionizing radiation, $d\bar{\varepsilon}$, in a mass of material, dm, in such interactions is quantified as absorbed dose, D, and it is expressed in energy (J) absorbed per unit mass (kg) – which has the unit of gray (Gy) [11]:

$$D = \frac{d\bar{\varepsilon}}{dm} \tag{1.1}$$

Over the years, many advances have been made with the main objective of increasing the dose delivered to the tumour whilst sparing surrounding healthy tissues. For instance, imaging techniques are more precise, allowing a more accurate tumour localisation, the treatment planning systems became computerized and new radiation types were introduced because of more favourable dose deposition characteristics. The advantage of proton therapy for tumour eradication relies on the finite range of these particles in tissue and it can be understood by comparing depth-dose distributions in water for distinct particles used in radiotherapy.

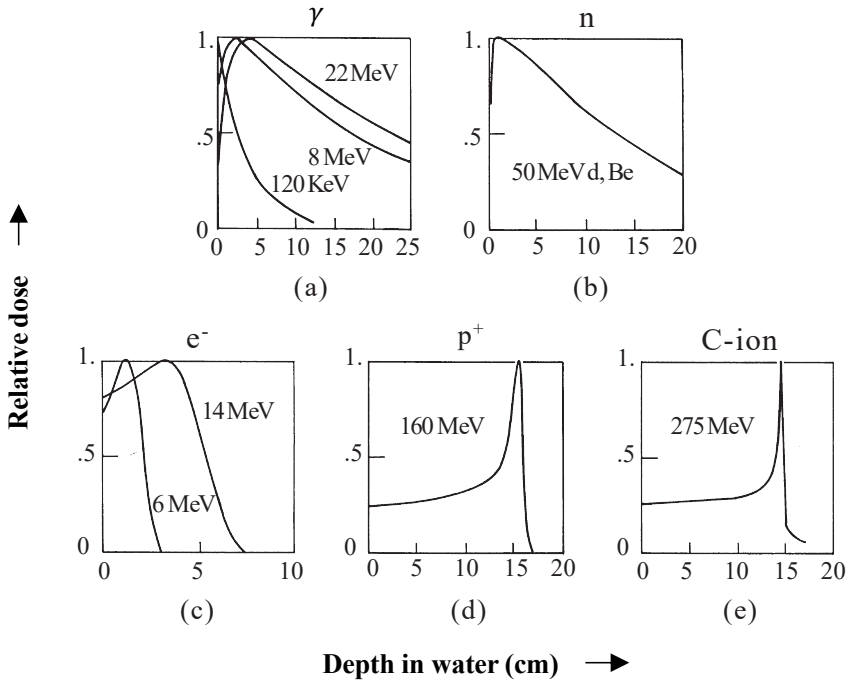

Figure 1.2: Depth-dose distribution curves in water for neutral particles, such as photons (a) and neutrons (b), and for charged particles, such as electrons (c), protons (d) and carbon-ions (d) [1].

Figures 1.2 (a) and (b) correspond to depth-dose curves of neutral particles. One can see that gamma rays and

neutrons show a short build-up region followed by an exponential-like decay in dose. As the absorbed dose is directly dependent of the particle fluence (number of particles per unit area), the dose can be seen to decrease exponentially as the fluence falls exponentially due to interactions with matter. For neutral particles, dose is not directly delivered to the medium, instead, these particles will interact in matter and release secondary electrons, which then proceed to deposit their energy in the medium. The secondary electrons will not deposit their energy immediately at the site they were produced and this is why the depth-dose curves show an initial build-up region. This aspect is particularly useful for radiotherapy as it allows one to spare the skin from undesirable high dose depositions. Figures 2 (c), (d) and (e) show characteristic depth-dose distribution curves for charged particles, arranged by increasing mass. Contrary to neutral particles, the fluence of charged particles only decreases slightly with depth. All charged particles lose their energy continuously and the rate of energy loss increases as these slow down, having a maximum energy deposition at the end of their track. The peak in dose is named as Bragg peak and it is sharper the heavier is the particle. The range of the particles and, therefore, the depth of the Bragg peak can be adjusted by varying the initial energy of the beam. One can see that the maximum dose peak for electrons is quite broad due to the small electron mass. For being light particles, these scatter more in matter. For heavier particles such as protons and carbon-ions, the peak is much sharper. This feature is the main advantage of the use of proton over photons in radiotherapy since one can point the maximum dose deposition to a tumour target whilst sparing the tissues behind it. Clinically, if a certain number of proton beams with different energies are produced in the same direction, distinct Bragg peaks will occur, as it is shown by the dashed curves in figure 1.3. The combination of these peaks produces the so-called Spread-Out Bragg peak (SOBP), represented by the solid line. The proton beam is modelled in such a way so that the maximum energy is deposited uniformly across the target volume defined by the dark grey region. For patient treatments, energies between 50 MeV and 250 MeV are used, which allows a penetration in tissue from a few millimetres up tp 40 cm. As the beam stops in tissue, dose is not delivered to healthy tissues located behind the tumour (light grey area), reducing the risks of long-term side effects. This type of therapy is particularly beneficial to children and young adults as their healthy tissues are still in development [1].

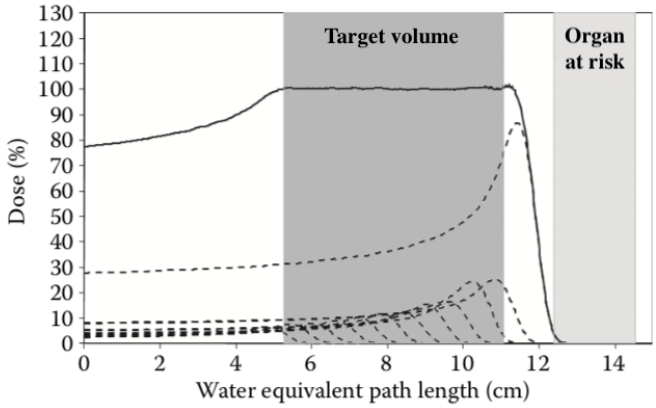

Figure 1.3: Schematic representation of a Spread-Out Bragg peak (solid line) obtained through the superposition of individual Bragg peaks (dashed lines) [1].

1.3 THE INTERNATIONAL MEASUREMENT SYSTEM – DOSIMETRY METROLOGY

Proton centres and radiotherapy units in general need to ensure that patients undergoing radiation treatment receive doses within internationally accepted levels of accuracy. To accomplish national and international uniformity in dosimetry metrology, user reference instruments should be traceable to Primary Standards either by direct calibration in a Primary Standard Dosimetry Laboratory (PSDL) or, more commonly, in a Secondary Standard Dosimetry Laboratory (SSDL), which in turn is linked to a PSDL. Only a small number of countries in the world are provided by PSDL for radiation

dosimetry so it is impossible for these to calibrate all dosimetry instruments used all over the world. For this reason, countries with national laboratories for primary standards calibrate secondary standards laboratories. The calibration chain for user reference instruments is illustrated in figure 1.4.

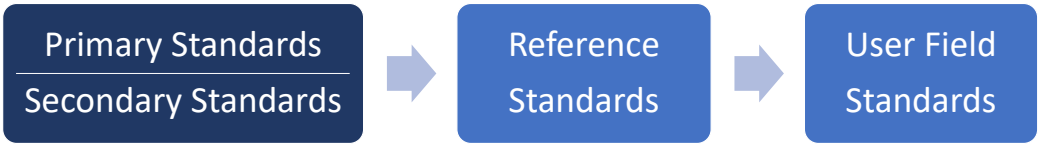

Figure 1.4: The calibration sequence for reference and user field dosimeters.

To better understand the calibration chain, it is necessary to distinguish between primary, secondary, reference and user field standards. To begin with, a primary standard is defined as an instrument of the highest metrological quality that allows to determine a unit of a quantity from its definition. The accuracy of a primary standard is established by comparing it with other standards of other institutions at the same level. On the other hand, a secondary standard is an instrument calibrated against a primary standard. The reference standard is defined as an instrument of the highest metrological quality accessible at a given location, from which measurements at that location are derived. Finally, the user field standard is the instrument used for routine measurements in radiotherapy centres, which is calibrated against the reference instrument at the site. In practice, radiotherapy units possess several field dosimeters for daily measurements and only one reference instrument. The reference instrument of the radiotherapy unit is normally sent to a PSDL or a SSDL where it is calibrated. It is important to note that the reference instruments at the PSDL or SSDL may not be directly calibrated against the primary or secondary standard. Instead, PSDLs and SSDLs calibrate hospitals' reference instruments against their own reference standards (the transfer standards), which in turn is calibrated against primary or secondary devices. This procedure is used because primary and secondary instruments are very sensitive and complex to operate, therefore it is not convenient to handle them often. Transfer standards are, in fact, considered part of the primary standards themselves and this system has proven to be highly consistent throughout the years.

In dosimetry, the quantity of interest is absorbed dose to water since water is the proxy for biological tissue. At PSDLs, the absolute value of this quantity can be determined via three basic techniques, which are calorimetry, chemical dosimetry or ionization dosimetry. At the National Physical Laboratory (NPL) in the United Kingdom, the primary standards of absorbed dose to water are determined using graphite calorimeters and operated in a Cobalt-60 gamma-ray beam quality, as well as in photon and electron beams. Currently, PSDLs do not have access to proton beams in their facilities. Usually, the reference instruments as well as user field instruments are ionization chambers [12].

At NPL, the general calibration chain begins with the direct determination of absorbed dose-to-water from a Cobalt-60 beam (beam quality Q_0), D_{water,Q_0}, using a graphite calorimeter. Afterwards, the exact same dose is delivered by the same beam quality to the reference dosimeter and its reading, M_{Q_0} is registered. The absorbed dose-to-water in the absence of the ion chamber, at the reference depth z_{ref} in a water phantom, for the beam quality Q_0, is related to the reference dosimeter's reading through the calibration coefficient of the dosimeter in terms of absorbed dose-to-water for the beam quality Q_0, $N_{\text{D,W},Q_0}$, and it is expressed by:

$$D_{\text{water},Q_0} = M_{Q_0} \cdot N_{\text{D,w},Q_0} \tag{1.2}$$

As mentioned above, PSDLs have no direct access to a proton beam in their facilities. This means that the reference instruments are calibrated in the reference beam quality, Q_0 – Cobalt-60 – which is different from the beam quality, Q, they are meant to operate in, which is, in this case, a proton beam. When two distinct beam qualities are involved, the equation of absorbed dose to water for the beam quality, Q, is given by:

$$D_{\mathrm{water},Q} = M_Q \cdot N_{D,w,Q_0} \cdot k_{Q,Q_0} \tag{1.3}$$

where M_Q is the chamber's reading in the proton beam, N_{D,w,Q_0} represents the calibration coefficient of the dosimeter in the reference beam quality Q_0 referred above and the factor k_{Q,Q_0} is the beam quality correction factor which corrects for the different response of the ionization chamber between the user beam quality Q and the calibration beam quality Q_0.

The beam quality correction factor can be obtained directly from calorimetry experiments by the ratio of the calibration coefficients in terms of absorbed dose-to-water at the qualities Q and Q_0. Because of the lack of proton beams in PSDLs, k_{Q,Q_0} are calculated analytically as:

$$k_{Q,Q_0} = \frac{(W_{\mathrm{air}}/e)_Q \cdot (s_{\mathrm{water,air}})_Q \cdot p_Q}{(W_{\mathrm{air}}/e)_{Q_0} \cdot (s_{\mathrm{water,air}})_{Q_0} \cdot p_{Q_0}} \tag{1.4}$$

where W_{air}/e is the energy required to produce an ion pair, $s_{\mathrm{w,air}}$ is the water to air stopping power ratio and p is the ionization chamber perturbation factor which accounts for the non-water equivalence of the air cavity and the chamber's wall. The equations (1.3) and (1.4) were first proposed by Hohlfeld [13] in 1988 for high-energy photon beams and established later for proton beams by Medin *et al.* [14] in 1995. The same methodology is employed in the IAEA TRS-398 code of practice, which is the reference protocol used in proton beams [12].

In proton beams, the beam quality correction factor, k_{Q,Q_0}, introduces an uncertainty of 4.2% (k=2) in the determination of absorbed dose-to-water. In fact, this is the main contribution to the uncertainty of $D_{\mathrm{water},Q}$, which is of the order of 4.6% (k=2), whereas an uncertainty of only 1.5% (k=2) is estimated for photon beams. The quantities that introduce the largest uncertainty in k_{Q,Q_0} are $s_{\mathrm{water,air}}$ and p [12].

1.4 AIM OF THE WORK – PROJECT OVERVIEW

The use of proton beams for radiotherapy has expanded in the last few decades. To use this technique to its full potential, uncertainties on reference dosimetry in proton therapy should be improved. This project aims to improve reference dosimetry by minimising the uncertainty in dose calculations caused by the non-water equivalence of the air cavity and entrance window of ionization chambers currently used worldwide in clinical proton therapy facilities. All available protocols for reference dosimetry in proton therapy consider ionization chamber perturbation factors, p, to be unity, although it is known from previous work that these perturbation factors can amount to 1% [15]. This contributes to uncertainties in the determination of absorbed dose-to water which is of the order of 4.6% (k=2) for proton therapy beams, compared to 1.5% (k=2) of uncertainty in photon therapy [12]. Ionization chamber perturbation factors are calculated by considering different geometries of the chamber at water-equivalent depths using FLUKA Monte Carlo (MC) code, which requires the development of code with detailed modelling of these detectors. Moreover, dosimetry calculations within MC codes are very sensitive to artifacts if the correct physics list are not used. The particle transport algorithms, the energy loss along the condensed history (CH) step and the boundary crossing events must be as accurate as possible. Therefore, the MC code used to perform the proposed calculations was evaluated through a self-consistency test, the so called Fano test.

2 INTERACTIONS OF CHARGED-PARTICLES WITH MATTER

In radiation dosimetry, it is crucial to understand in detail the mechanisms of radiation interactions with matter in order to characterise, as accurate as possible, the energy deposition in a biological tissue [2]. Charged particles have an electric field, thus the process of energy loss for these particles is mainly based on electromagnetic or Coulomb interactions with atomic electrons and nuclei. In addition to electromagnetic interactions between charges, heavy charged particles can occasionally undergo head-on collisions with atomic nuclei (non-elastic nuclear interactions), which alter the beam fluence by changing the nature of the projectile, decreasing the primary beam fluence, and setting secondary particles in motion, discussed in section 2.3.

Electrons and positrons present a mass value much smaller in comparison with other charged particles. This influences the amount of energy transferred in one collision with matter, as well as the scattering angles. For this reason, it is suggested to consider these lighter particles in a different category from charged particles heavier than electrons. Although the aim of this work is to study proton beams, secondaries such as other heavy charged particles and electrons are considered since they result from proton interactions. Thus, an overview of charged particle interactions with matter is presented.

2.1 PHYSICS OF PARTICLE INTERACTIONS

Charged particles interact with atomic electrons and nuclei as they pass through matter. These interactions result in energy losses and scattering of the projectiles along their track and also in excitation and ionization of the atoms in the medium. Each of these interactions is assigned a specific cross section σ, i.e., the probability of a particular interaction. Charged-particle Coulomb interactions are divided into four categories based upon the relationship between the classical impact parameter b - defined as the distance between the projectile and the atom's centre - and the atomic radius, r [16]. These four types of interactions are shown in figure 2.1 and the description of each situation is generalised for all charged particles, however, some occur more frequently for either light or heavy particles.

$b \ll r$: Elastic and inelastic radiative interactions

In the cases presented in sub-figures 2.1 (a) and 2.1 (b), the impact parameter, b, is much smaller than the radius, r, of the atom in the medium, which means that the projectile interacts mainly with the atomic nucleus. Electromagnetic interactions of charged particles with the external nuclear field result in either elastic or inelastic scattering. Elastic interactions are the most frequent and are characterized by the deflection of the projectile's trajectory by the nucleus, especially in high-Z materials. When a beam of particles traverses a slab of material, it diverges due to the particles' deflection by the atomic nuclei. The lighter is the projectile, the larger are the deflections. In fact, this is the main mechanism by which electrons scatter. However, the scattering angles due to a single collision are typically very small therefore the increasing cross sectional area of the beam is a result of *multiple Coulomb scattering* (MCS). In order to conserve the momentum in a collision, the projectile loses a small amount of its initial kinetic energy, which is extremely small for the therapeutic energy range, and the target atom does not suffer excitation nor ionization. For example, for heavy charged particles, this type of collision contributes minimally, less than 1%, to the total energy loss, unless for particles with energies below several tens of keV [17].

In contrast, during inelastic radiative interactions, the incident particle may undergo a significant energy loss, with the emission of a x-ray (*bremsstrahlung*) photon or provoke an excited state in the nucleus. In fact, *bremsstrahlung* radiation does not occur exclusively upon interactions with the nucleus. This type of radiation can also be emitted upon interactions with the Coulomb field of atomic electrons [18].

For both elastic and inelastic radiative types, the interaction cross section depends on the square of the atomic number (Z^2) of the target material. Furthermore, the inelastic radiative interaction cross section is inversely proportional to the square of the charged particle's mass ($1/M^2$), thus, radiative energy loss can be considered negligible for incident

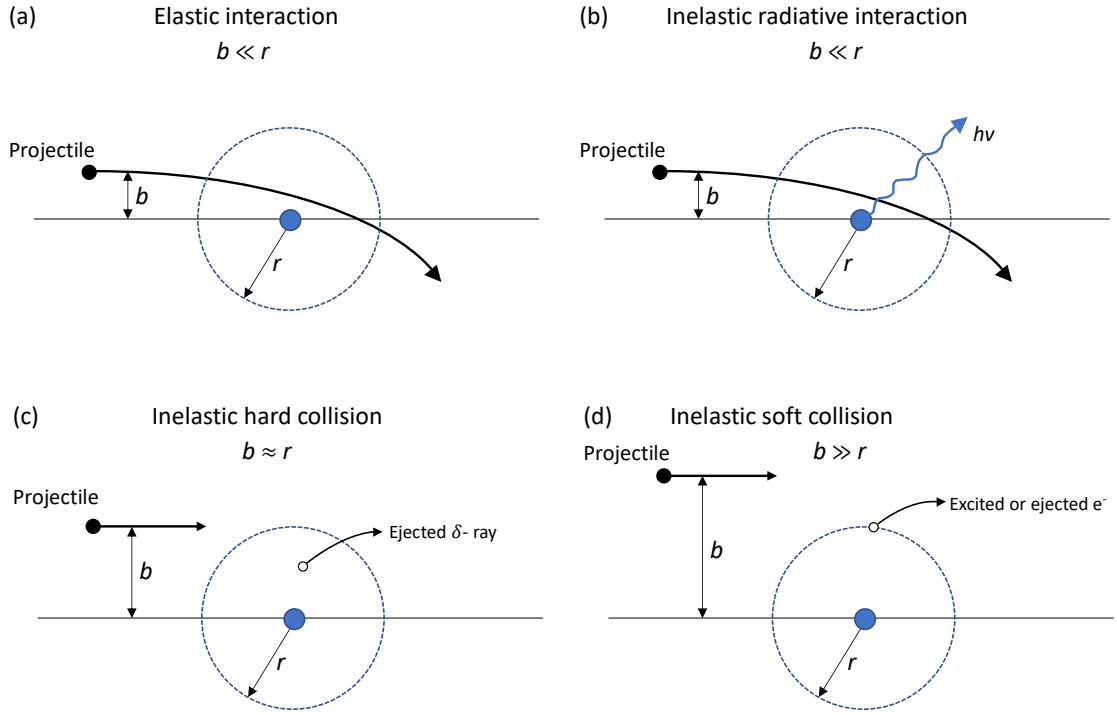

Figure 2.1: Schematic illustration of the different types of interactions of charged particles with a target atom, based on the comparison of the impact parameter, b, relative to the atomic radius, r. Elastic (a) and inelastic radiative (b) interactions for $b \ll r$, and inelastic hard (c) and soft (d) interactions, $b \approx r$ and $b \gg r$, respectively [2].

particles heavier than electrons or positrons.

***b* ≈ *r*: Inelastic hard collision**

In the sub-figure 2.1 (c), the impact parameter of the projectile is similar to the atomic radius of the absorber material. In this situation, the charged particle is more likely to interact directly with a single atomic electron, commonly from an inner shell, transferring part of its energy to the electron. Typically, the energy transferred is much larger than the electron's atomic binding energy, therefore, hard collisions can be approximated as interactions between the charged projectile and a free electron. Upon this interaction, the electron, now referred to as a *delta-ray (δ-ray)*, is ejected from the atom with a significant kinetic energy, enough to undergo its own interactions with the medium and to deposit its energy along a different track from the primary charged particle. The probability for inelastic hard collisions between charged particles and electrons is small. The energy loss depends on the type of the incident particle. Light projectiles, for instance, could lose a significant amount of its kinetic energy in this type of interaction.

***b* ≫ *r*: Inelastic soft collision**

Sub-figure 2.1 (d) shows the projectile interacting with the atom as a whole, since the impact parameter of the charged particle is much larger than the atomic radius. These interactions are characterized by small energy transfers and the main resulting effects are excitation and ionization of the atoms in the medium. Even though the energy transferred to the atom is of the order of a few eV, inelastic soft collisions are by far the most frequent, therefore the charged particle could lose around 50% of its kinetic energy to the medium [19]. The energy transferred by a particle undergoing hard and soft collisions are the most impactful mechanisms for energy loss.

2.2 STOPPING POWER

Charged particles traversing a medium will undergo the interactions described above with the atoms of the material, losing their energy along their track, until they stop in the medium. The average energy loss, dE, per unit path length, dx, is defined as the linear stopping power, S, of the traversed material and it is expressed in MeV/cm:

$$S = -\frac{dE}{dx} \tag{2.1}$$

A commonly used quantity is the mass stopping power, $-(1/\rho)dE/dx$, which has units of MeV·cm^2/g. This quantity is usually preferred due to its low dependence on the density of the traversed material [20]. For heavy charged particles, depending on the mechanisms of particles interactions, one can distinguish two components of the total stopping power: electronic (el), also called collision (col), and nuclear (nuc) stopping powers (equation 2.2). The former results from interactions of charged particles with atomic electrons. It includes both inelastic hard and soft collisions and it is the main contribution to the total stopping power. With regards to the nuclear stopping power, it only includes energy losses due to elastic interactions between the projectile and the atomic nuclei of the target, as inelastic radiative interactions are only relevant for electrons and positrons.

$$-\frac{1}{\rho}\left(\frac{dE}{dx}\right)_{\text{total}} = -\frac{1}{\rho}\left(\frac{dE}{dx}\right)_{\text{el}} - \frac{1}{\rho}\left(\frac{dE}{dx}\right)_{\text{nuc}} \tag{2.2}$$

For electrons and positrons, the total stopping power accounts the contribution of the collision (col), also called electronic (el), and the radiative (rad) stopping powers (equation 2.3). The former includes the same type of interactions as described above for heavy charged particles. The radiative stopping power includes all inelastic energy losses in which *bremsstrahlung* radiation is emitted.

$$-\frac{1}{\rho}\left(\frac{dE}{dx}\right)_{\text{total}} = -\frac{1}{\rho}\left(\frac{dE}{dx}\right)_{\text{col}} - \frac{1}{\rho}\left(\frac{dE}{dx}\right)_{\text{rad}} \tag{2.3}$$

2.2.1 THE CONTRIBUTIONS TO THE TOTAL STOPPING POWER

The calculation of the energy loss to atomic electrons due to interactions of heavy charged particles and electrons was first introduced by Bohr using classical arguments. This quantity was later extended to quantum mechanics by Bethe, Bloch and others [21].

- **Heavy charged particles**

  For charged particles heavier than electrons and positrons, the nuclear component of the stopping power is negligible, especially for the therapeutic energy range, thus $S_{total} \approx S_{el}$. According to the ICRU Report 49, S_{el} is calculated as the sum of energy loss due to both hard and soft collisions [17]. This is formulated as follows:

$$\frac{1}{\rho}S_{el} = \frac{4\pi r_e^2 m_e c^2}{u}\frac{1}{\beta^2}\frac{Z}{A}z^2 \cdot \left[\ln\left(\frac{2m_e c^2\beta^2}{I}\right) - \ln(1-\beta^2) - \beta^2\right] \tag{2.4}$$

  where r_e represents the classical electron radius, $m_e c^2$ the electron rest mass energy, u the atomic mass unit, β is the velocity of the incident charged particle as a fraction of the speed of light ($\beta = v/c$), Z/A is the ratio of number of electrons per molecular weight of the medium and z the projectile charge. In the logarithmic factor, I is the mean excitation energy of the medium.

- **Electrons and positrons**

  For electrons, the collision stopping power expression differs from the one presented for heavy particles since the energy loss due to soft collisions has a different formulation for these particles. According to the ICRU Report 37 [18], the mass collision stopping power for electrons is written as follows:

$$\frac{1}{\rho}S_{col} = \frac{2\pi r_e^2 mc^2}{u}\frac{1}{\beta^2}\frac{Z}{A}\cdot\left[\ln\left(\frac{E_k^2}{I^2}\right)+\ln\left(1-\frac{\tau}{2}\right)+F^-(\tau)\right] \tag{2.5}$$

  where E_k is the kinetic energy of the incident electron and $\tau = E_k/m_e c^2$. The function $F^-(\tau)$ is expressed as:

$$F^-(\tau) = (1-\beta^2)\left[1+\frac{\tau^2}{8}-(2\tau+1)\ln 2\right] \tag{2.6}$$

  Contrary to heavy charged particles, when calculating the total stopping power for electrons or positrons, it is important to take into account the radiative component, particularly at higher kinetic energies. The general expression for the mass radiative stopping power is given as:

$$\frac{1}{\rho}S_{nuc} = N_a \Phi_{rad} E_0 \tag{2.7}$$

  where N_a represents the number of atoms per unit mass in the traversed medium, Φ_{rad} is the cross section function for *bremsstrahlung* production, which is a function that depends on Z and also on E_0, being E_0 the initial total energy of the electron or positron; the function Φ_{rad} depends on the kinetic energy of the light particle and has different formulations for non-relativistic, relativistic and high-relativistic energy ranges [19].

The most relevant feature in the mass electronic stopping power formulas for both heavy and light charged particles is the inverse dependence on the velocity of the incident particle, β. This aspect translates the increase in energy loss as the particle slows down. Several corrections were added to both original formulations later, such as the density effect, (δ), and shell, (C), corrections [22]. The former accounts for polarization effects, specially in solid media and it only becomes relevant at high energies. The shell correction becomes important at low energies, when the velocity of the projectile is lower than the velocity of orbital electrons of the atoms in the medium.

2.2.2 RESTRICTED ELECTRONIC STOPPING POWER

In dosimetry, it is of interest to measure the energy deposited by charged particles in a specific region, usually referred as cavity. The detectors used for these measurements are usually ionization chambers. As mentioned above, the electronic or collision stopping power is the energy loss by charged particles to atomic electrons, S_{el}, and it includes both hard and soft collisions. However, δ-rays ejected in hard collisions could be energetic enough to escape the region of interest and therefore deposit their kinetic energy outside the cavity. Due to this effect, it was introduced a new quantity known as the restricted stopping power, L_Δ. The latter does not account for the energy loss by δ-rays with energies higher than a certain threshold Δ, which is established depending on the cavity size [16]. The original electronic stopping power is now called the unrestricted electronic stopping power and it is larger than the restricted stopping power as it overestimates the energy loss by charged particles as it considers that all δ-rays deposit their energy locally. Note that it is meaningless to establish a Δ value greater than the maximum energy transferred to an atomic electron in a hard collision, $E_{\max,\Delta}$. The lower the threshold, the larger is the divergence between restricted and unrestricted stopping powers. As one increases Δ, the disparities become lower and when $\Delta = E_{\max,\Delta}$, the restricted stopping power is equal to the unrestricted stopping power.

Figure 2.2 illustrates the unrestricted mass electronic stopping power (solid line) and the restricted mass electronic stopping powers for thresholds of Δ=10 keV (dotted line) and Δ=100 keV (dashed line) as a function of the kinetic energy of electrons in water. All curves were obtained through Monte Carlo (MC) simulations, using the FLUKA MC code [23, 24]. In order to analyse the discrepancies between unrestricted and restricted stopping powers and the respective threshold values, it is important to have an idea of $E_{\max,\Delta}$. The maximum energy transferred depends on the incident charged particle. For instance, electrons transfer up to half of their kinetic energy to δ-rays. This means that for a fixed value of energy transfer Δ, the electron must have a minimum kinetic energy of 2Δ to produce a δ-ray. Therefore, for kinetic energies up-to 2Δ the unrestricted and restricted stopping powers coincide whereas for kinetic energies higher than 2Δ the restricted stopping power becomes lower. This is shown in figure 2.2 where, for Δ=10 keV and Δ=100 keV, the restricted stopping power starts to diverge from the unrestricted stopping power at 20 keV and 200 keV, respectively.

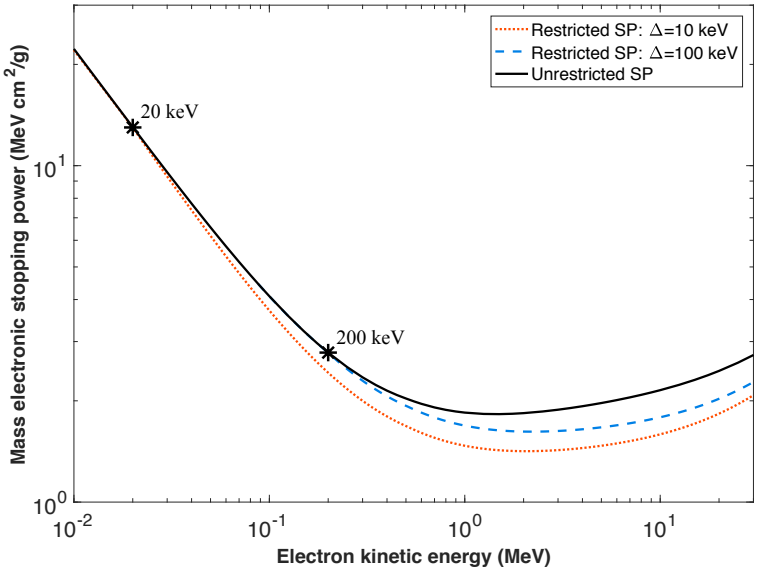

Figure 2.2: Variation of the unrestricted mass electronic stopping power and restricted mass electronic stopping powers for Δ=10 keV and Δ=100 keV for electrons in water. Adapted from Andreo *et al.* [2].

Figure 2.3 shows the same curves as described above for the case of protons. The minimum energy that protons must have in order to produce a 10 keV and a 100 keV δ-ray is 4.59 MeV and 45.9 MeV respectively. This energy can be calculated according to the following expression:

$$E = \frac{1}{4} \cdot \frac{(M+m)^2}{M \cdot m} \cdot E_{\text{transf}} \tag{2.8}$$

where $M = 1.673 \times 10^{-27}$ kg is the proton mass, $m = 9.109 \times 10^{-31}$ kg is the electron mass and $E_{\text{transf}} = \Delta$, which is the maximum energy transfer to the electron. For Δ=10 keV and Δ=100 keV, the restricted stopping power starts to diverge from the unrestricted stopping power at 4.59 MeV and 45.9 MeV, respectively.

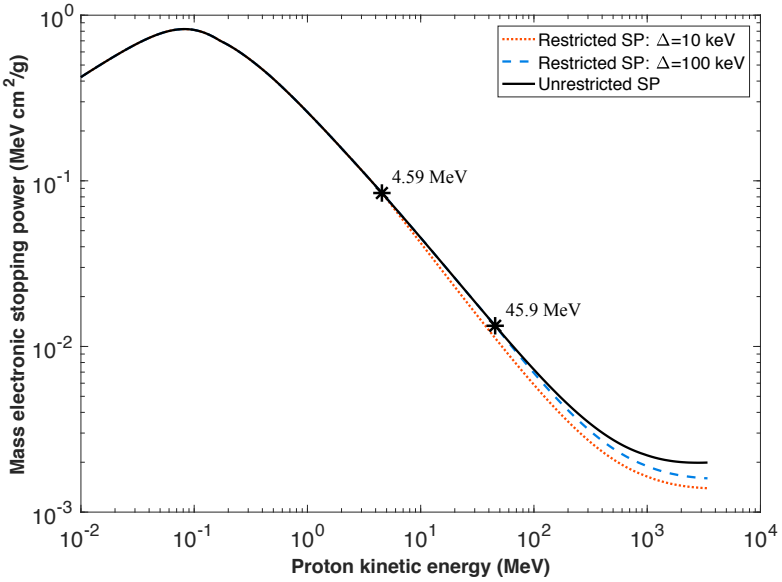

Figure 2.3: Variation of the unrestricted mass electronic stopping power and restricted mass electronic stopping powers for Δ=10 keV and Δ=100 keV for protons in water.

2.3 NUCLEAR INTERACTIONS OF PROTONS

In addition to Coulomb interactions with atomic electrons and the nuclear electric field, heavy charged particles may undergo the so called non-elastic nuclear interactions [25]. For the specific case of a proton beam, in such interactions, a proton may enter into the nucleus of a target atom to form an excited system which is later fragmented resulting in secondary particles such as protons, that includes also the primary proton since it is no longer distinguishable, neutrons or lighter fragments of the nucleus. Even though these interactions are considered to be rare when compared to electromagnetic interactions, they are not negligible and must be taken into account. For a 60 MeV proton beam, about 4% of the primary protons are lost before stopping due to non-elastic nuclear interactions [26]. The decline in the number of primary protons is higher as the energy of the beam increases so that, for instance, a 160 MeV proton beam, loses almost 20% of its primary protons in this type of interaction [1]. For a 250 MeV proton beam, the number of primary protons decreases in such a way that the peak-to-plateau ratio of dose decreases by a factor of 40% [27]. Therefore, to perform accurate studies with proton beams it is of great importance to consider non-elastic nuclear interactions and consider the secondary particles generated in these interactions.

The secondary charged particles resulting from non-elastic nuclear interactions could be secondary protons, deutrons, tritons, helions and alphas; from these interactions could also result neutrons as well as gamma rays.

3 PROTON DOSIMETRY

The dosimetry field can be divided into absolute and relative dosimetry. The first is characterized as the fundamental measurement of absorbed dose in a medium with a detector, without need for calibration of the detector's response. The latter derives from the former, which means that relative dosimeters must be calibrated against absolute systems [19]. As mentioned previously, three different techniques are used for absolute dosimetry in PSDL, which are calorimetry, chemical dosimetry and ionization dosimetry. Only calorimetric dosimetry will be discussed in the next section since this is the primary standard method used at NPL for photon and particle beams.

3.1 GRAPHITE AND WATER CALORIMETRY

Calorimetric dosimetry is based on measuring the temperature rise in a medium as a result of energy deposition by ionizing radiation. The instrument used for calorimetry measurements is known as a calorimeter and it contains a small cavity, the sensitive volume, in which dose is to be determined. The point of measurement is thermally insulated from the exterior materials and it incorporates a temperature sensor, i.e. a thermistor. When the calorimeter is irradiated, only a fraction of the energy transported by the beam's particles is transferred and deposited in the medium, resulting in the temperature rise measured. The resulting thermal energy, ΔQ, in the point of measurement is expressed by:

$$\Delta Q = m \cdot c \cdot \Delta T \tag{3.1}$$

where m refers to the mass of the medium, c is the specific heat capacity of the medium expressed in J kg^{-1} K^{-1} and ΔT is the temperature rise in the medium. Assuming that all energy deposited in the calorimeter's core is converted into heat, the equation above can be rearranged in terms of absorbed dose in the medium:

$$\frac{\Delta Q}{m} = D = c \cdot \Delta T \tag{3.2}$$

In radiation dosimetry, the quantity of interest is absorbed dose to water, so water would be the ideal medium for a calorimetry system. According to NIST, the specific heat capacity of water is 4186 J kg^{-1} K^{-1}. In a radiotherapy context, doses of the order of 2 Gy are delivered to patients in each fraction, therefore the rise in temperature in a water calorimeter would be of the order of 0.5 mK. It is undeniable that such a small increase in temperature is extremely hard to measure and this is clearly the major disadvantage of water calorimetry. Water calorimeters are used for absolute dose measurements, but these are not convenient for routine measurements because of their lack of sensitivity and complexity of operation. The difficulty with water calorimeters is due to the high specific heat capacity of water. If water could be replaced by another material with lower specific heat, the temperature rise per unit dose will increase - since, as shown in equation 3.2, ΔT is inversely proportional to c. As an alternative to water, graphite is often used as the medium of interest in calorimetry. According to NIST, the specific heat capacity of graphite is 710 J kg^{-1} K^{-1}, which is about 6 times smaller than that of water, therefore the increase in the medium's temperature is around 6 times larger. Subsequently, for the same dose of 2 Gy, the rise in temperature in a graphite calorimeter is approximately 2.8 mK. Although this temperature rise is significantly larger and therefore relatively easier to measure than the one for water, graphite is not as tissue equivalent as water, despite having similar atomic numbers. This means that the obtained quantity, which is absorbed dose-to-graphite, needs to be converted into absorbed dose-to-water through conversion factors. The latter introduces larger uncertainties in the determination of absorbed dose-to-water in comparison with water calorimetry [19, 28].

To conclude, some PSDLs use water calorimeters whereas others use graphite calorimeters for absolute dose determination in photon and particle beams. Clearly, both water and graphite calorimeters have advantages and disadvantages and different PSDLs have developed expertise in a specific type of calorimeter. Calorimeters are complex,

not commercially available and hard to operate; therefore, these are only developed at PSDLs.

3.2 IONIZATION CHAMBER DOSIMETRY

Reference instruments discussed in section 1.3 are classified as a relative dosimetry system since these must be calibrated against absolute standards. Relative dosimetry is a wide field, unlike absolute dosimetry. Many different techniques can be used depending on the application, although the most common and practical reference dosimetry instrument to measure the output of proton treatment systems and determine absorbed dose is an air-filled ionization chamber [29].

3.2.1 CAVITY THEORY

To measure the dose delivered in a water phantom, it is necessary to introduce a dosimeter into the medium. Dosimeters that are widely used for dose measurements in proton beams are ionization chambers whose sensitive volume, usually referred to as the cavity, is air. The relation between the absorbed dose in the air cavity of the ionization chamber and the absorbed dose in the material of the phantom is based on Bragg-Gray (BG) and Spencer-Attix (SA) cavity theories. The Bragg-Gray cavity theory was first established for photon beams but it can be directly applied to charged particles beams such as protons. The theory relies on the following assumptions [30]:

1. The cavity is small compared to the range of the charged particles so that their fluence in the medium is not altered by the presence of the air cavity. As a result, the fluence in the medium is the same as in the air cavity for all particles present in the beam;
2. All charged particles that deposit dose in the cavity, cross the cavity completely. This implies that no particles will stop in the cavity and no secondary particles will be produced inside the cavity;
3. *Bremsstrahlung* radiation is insignificant, therefore it does not contribute to the total dose in the cavity.

Considering that the above conditions are satisfied, the absorbed dose in the medium, D_{medium}, relates to absorbed dose in the air cavity, D_{air}, through the unrestricted mass electronic stopping power ratio of the medium and air, $s^{\mathrm{BG}}_{\mathrm{medium,air}}$:

$$D_{\mathrm{medium}} = D_{\mathrm{air}} \cdot s^{\mathrm{BG}}_{\mathrm{medium,air}} \tag{3.3}$$

where $s^{\mathrm{BG}}_{\mathrm{medium,air}}$ is expressed in equation 3.4. Note that a proton beam contains primary protons as well as secondary charged particles. The transport of each type of particle must be treated separately and added, as represented by $\sum_i$.

$$s^{\mathrm{BG}}_{\mathrm{medium,air}} = \frac{D_{\mathrm{medium}}}{D_{\mathrm{air}}} = \frac{\sum_i \int_0^{E_{\max}} \Phi^i_{\mathrm{medium}}(E)(S(E)/\rho)^i_{\mathrm{medium}} dE}{\sum_i \int_0^{E_{\max}} \Phi^i_{\mathrm{air}}(E)(S(E)/\rho)^i_{\mathrm{air}} dE} \tag{3.4}$$

where i represents the type of charged particle in the beam, $E_{\max}$ is the maximum kinetic energy of the particle, $\Phi_{\mathrm{medium}}(E)$ and $\Phi_{\mathrm{air}}(E)$ are the fluence differential in energy in the medium and air, respectively, S/ρ is the mass unrestricted stopping power. Under the conditions of Bragg-Gray, $\Phi_{\mathrm{medium}}(E) = \Phi_{\mathrm{air}}(E)$.

Experimental results showed that the proposed relation, in equation 3.3, did not predict accurately the ionization in air cavities [16]. Spencer and Attix refined the cavity theory to include $\delta-$ray production in the cavity and considered the restricted mass electronic stopping power ratio between water and air - $s^{\mathrm{SA}}_{\mathrm{water,air}}$. The calculation of this quantity will be discussed in section 5.3.

Both cavity theories are valid under the assumption that particle fluence does not change with the presence of the air cavity, or the whole detector, in the medium. In fact, this would be the case if the detector would be made of the same material, in terms of atomic composition and density, as the medium in which it is placed. Despite the effort to develop medium equivalent materials to build the detectors, there is still notable perturbation in the fluence of charged particles. To account for this deviation from the ideal Bragg-Gray conditions defined above, a fluence perturbation correction factor, p, should be added to equation 3.3 [31]:

$$D_{\text{medium}} = D_{\text{air}} \cdot s_{\text{medium,air}} \cdot p \tag{3.5}$$

where $s_{\text{medium,air}}$ is the BG or SA medium-to-air stopping power ratio.

3.2.2 IONIZATION CHAMBER FUNCTIONALITY

Ionization chambers rely on the collection of ions which are produced when ionizing radiation passes through the sensitive volume, in this case the air cavity. Interactions of the radiation cause ionization and excitation of the gas molecules along the ionizing particle track. After a neutral molecule is ionized, the electrons attach to oxygen molecules to form negative oxygen ions [32]. The resulting positive and negative ions are called an ion pair. The operation of an ion chamber is then based on the collection of all charges created within the cavity through the application of an electric field between two electrodes. Positive and negative ions move to the electrodes of opposite polarity. The electrodes may be in the form of parallel plates, a cylinder or a sphere.

In this work, a plane-parallel plate ionization chamber is used, therefore the general composition of this type is described. Figure 3.1 is a simplified diagram of a plane-parallel plate ionization chamber. The cavity volume, which is filled with air, is bordered by the polarizing, collecting and guard electrodes. The polarizing electrode establishes the electric field in the air cavity since it is directly connected to the power supply. The collecting electrode is connected to the guard and has the function of collecting the produced charges, which is then measured by an electrometer. The electrometer must be capable of measuring very small output current which is of the order of femtoamperes to picoamperes, depending on the chamber design, radiation dose and applied voltage. The guard electrode, also called the guard ring, limits the sensitive volume of the chamber and avoids leakage current of the chamber to be collected by the collecting electrode [19, 33].

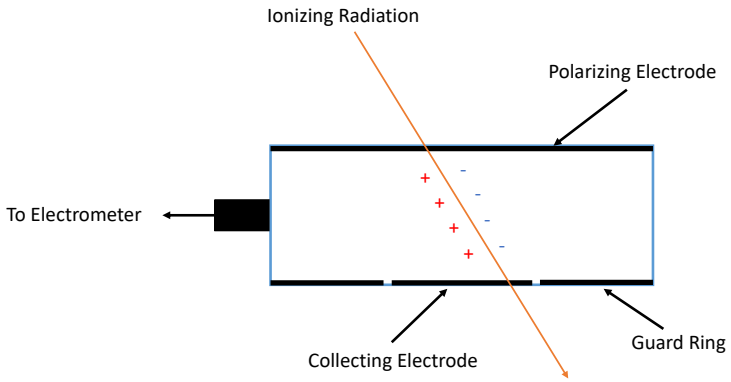

Figure 3.1: Schematic diagram of the composition of a plane-parallel plate ionization chamber.

According to the reciprocity theorem, if a small detector is used in a broad beam of a specific size or if a large sensitive area detector of a specific size is used with a small beam, the same results are obtained, if both source and detector are located in a homogeneous medium [16]. In spot scanning proton therapy systems, protons are delivered in very narrow beams (the so called pencil beams). Large detectors are thus often used for relative dosimetry measurements.

Ideally, these detectors would be used for dose reference measurements, however, PSDLs do not provide calibration coefficients ($N_{\mathrm{D,w},Q_0}$) for large area chambers. The latter are routinely used in the clinic for percent depth-dose and range measurements and small area chambers are typically used for dose reference measurements.

For an air-filled ionization chamber irradiated by a proton beam of quality Q, the average dose-to-air is given by:

$$\bar{D}_{\mathrm{air},Q} = \frac{M_Q \cdot (W_{\mathrm{air}}/e)_Q}{\rho_{\mathrm{air}} \cdot V_{\mathrm{cavity}}} \tag{3.6}$$

where M_Q represents the measured charge in the cavity, $\rho_{\mathrm{air}} \cdot V_{\mathrm{cavity}}$ is the mass of air in the cavity and $(W_{\mathrm{air}}/e)_Q$ is the mean energy required to produce an ion pair in air.

Dose-to-water can be simply obtained with an ionization chamber by applying Bragg-Gray (or Spencer-Attix) cavity theory. Thus, dose-to-water, $D_{\mathrm{water},Q}$, in a proton beam of quality Q is proportional to the average dose-to-air in the air cavity volume, $\bar{D}_{\mathrm{air},Q}$, by:

$$D_{\mathrm{water},Q} = \bar{D}_{\mathrm{air},Q} \cdot (s_{\mathrm{water,air}})_Q \cdot p_Q \tag{3.7}$$

where $s_{\mathrm{water,air}}$ is the Bragg-Gray (or Spencer-Attix) mass collision stopping power ratio between water and air for the charged particles spectrum at the measurement point in water and p_Q is the perturbation correction factor to account for deviations from the conditions under which Bragg-Gray cavity theory is valid.

Replacing the extended form of the average dose-to-air in equation 3.6, an overall expression for dose-to-water is obtained:

$$D_{\mathrm{water},Q} = \left[M_Q\right] \cdot \left[\frac{1}{\rho_{\mathrm{air}} \cdot V_{\mathrm{cavity}}}\right] \cdot \left[(W_{\mathrm{air}}/e)_Q \cdot (s_{\mathrm{water,air}})_Q \cdot p_Q\right] \tag{3.8}$$

It is important to highlight that the air cavity volume of commercial ionization chambers is not known accurately so it can be calculated through the following expression:

$$\frac{1}{\rho_{\mathrm{air}} \cdot V_{\mathrm{cavity}}} = \frac{N_{\mathrm{D,w},Q_0}}{(W_{\mathrm{air}}/e)_{Q_0} \cdot (s_{\mathrm{water,air}})_{Q_0} \cdot p_{Q_0}} \tag{3.9}$$

where $N_{\mathrm{D,w},Q_0}$ is the calibration coefficient of the dosimeter in terms of absorbed dose-to-water in the beam quality Q_0, which is the reference beam quality, usually taken to be a Cobalt-60 beam. Note that all quantities in this equation refer to the beam quality Q_0. By substituting equation 3.8 into the equation 3.7, dose-to-water can be expressed in the same form as presented in the IAEA TRS-398 (section 1.3):

$$D_{\mathrm{water},Q} = M_Q \cdot N_{\mathrm{D,w},Q_0} \cdot \frac{(W_{\mathrm{air}}/e)_Q \cdot (s_{\mathrm{water,air}})_Q \cdot p_Q}{(W_{\mathrm{air}}/e)_{Q_0} \cdot (s_{\mathrm{water,air}})_{Q_0} \cdot p_{Q_0}} \tag{3.10}$$

with:

$$\frac{(W_{\mathrm{air}}/e)_Q \cdot (s_{\mathrm{water,air}})_Q \cdot p_Q}{(W_{\mathrm{air}}/e)_{Q_0} \cdot (s_{\mathrm{water,air}})_{Q_0} \cdot p_{Q_0}} = k_{Q,Q_0} \tag{3.11}$$

where k_{Q,Q_0} is the beam quality correction factor.

4 MONTE CARLO IN RADIATION DOSIMETRY

4.1 GENERAL ASPECTS OF MONTE CARLO METHODS

The Monte Carlo (MC) method is a numerical and statistical approach based on random number sampling and it was developed to study and solve equations or integrals that occur in various branches of natural sciences [34]. In medical physics, it is applied in areas of research that involve studies of ionizing radiation interactions with matter, such as nuclear medicine, radiation diagnosis, therapy and protection [35].

4.1.1 RANDOM NUMBER GENERATORS

MC techniques use programs, known as random number generators (RNG), to compute huge sequences of pseudo random numbers, that must be uncorrelated within the sequence. They are referred to as pseudo random numbers because the output of any computer program is predictable. However, throughout of this section these numbers will be treated as purely random numbers. There are two requirements for a RNG. First, to avoid correlation between the numbers, the output sequence of N numbers should be large enough so it is not reused. Second, the N numbers should to be uniformly distributed in an n-dimensional space. However, in a radiation therapy context, one is not interested in uniformly distributed random numbers. Instead, it is relevant to generate random numbers according to probability distribution functions $p(x)$, which represent the probability of an interaction of any type happening when a particle passes through matter. Considering that a RNG generates uniformly distributed numbers η in the interval [a,b], it is possible to make use of the RNG to obtain random numbers distributed according to $p(x)$. There are two different approached for this purpose, the inverse transform and acceptance-rejection methods. The description of these methods is out of the scope of this thesis, please refer to Andreo [36] and Seco *et al.* [37] for a detailed description.

4.1.2 CONDENSED HISTORY FOR CHARGED PARTICLE TRANSPORT

When addressing problems using MC techniques, one must recreate/mimic the system of study. In radiation dosimetry, it is necessary to reproduce the real physical system, which could be a detector, a phantom or, more commonly, a combination of both. Particles of interest are produced and will interact with matter. The interactions with the physical system are based on probabilities of occurrence, i.e. interaction cross sections, and are governed by probability distribution functions, $p(x)$. However, charged particles undergo a very large number of interactions along their track, therefore the simulation of each particle history would be extremely time consuming. Luckily, most of these interactions are elastic, meaning that practically no energy or small amounts of energy are transferred to matter. Besides that, particles suffer very small scattering angles. These two characteristics enable one to group many of the interaction events into one, the so called, Condensed History step (CH), which can be seen as the solid line in Figure 4.1. CH is an approximate approach of charged particle transport, thus it is important to restrain the maximum distance travelled in one CH step – the step size parameter.

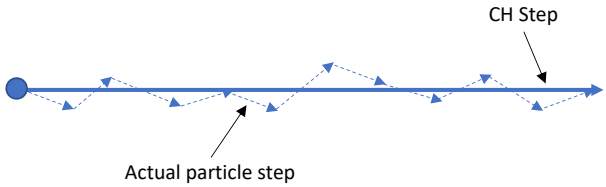

Figure 4.1: Simulated particle track using the CH technique (solid line) compared to a possible real particle path (dashed line).

Several interactions of a charged particle in a medium grouped into a CH step of length ds are translated in

continuous energy losses. The average energy lost by the particle and the total deflection resulting from multiple scattering in one CH step are determined through random number sampling. The estimated solution of these problems converges to the real solution as the number of histories, N (N random numbers), tends to infinity and the uncertainty of the result is proportional to $1/\sqrt{N}$ [37].

The CH technique works well primarily in homogeneous regions. However, it could present several artefacts at boundaries between media of different densities. Artefacts are especially visible when the distance to the next material boundary is smaller than the particle step. The solution for these problems consists of decreasing the step size when particles are close to a material interface.

Each of the simulated particles is followed from the point it is produced until it escapes the geometry of interest or until it loses a great fraction of its initial energy, reaching a cut-off energy value, E_{cut}, which is defined by the user. In order to have a close estimation of the behaviour of the real physical system, a large number of histories must be simulated. The output of a MC simulation is based on the statistical mean of the behaviour of the simulated particles. The overall uncertainty emerging from a MC simulation can be divided into uncertainties of type A and type B. Type A uncertainties are related to statistical uncertainties which depend on the number of histories simulated. The higher the number of particles in the simulation, the more precise is the calculated result, however, there is always a compromise between the level of statistical precision required and the computation time. This uncertainty does not inform the user about the accuracy of the result compared to the true physical solution [35]. On the contrary, uncertainties of type B include uncertainties related to the physical models implemented and data used in the code, as well as to the transport algorithms. The physical models and physical data can be checked by benchmarking against experimental results. Uncertainties in the particle transport algorithms in the computation of ionization chamber response are evaluated through a self-consistency test, known as the Fano cavity test [37], which is discussed in the section below.

4.2 THE FANO TEST

Dosimetry calculations with MC are specially sensitive to boundary crossing artifacts due to particle transport through multiple regions with varying densities. In fact, when simulating particles traversing an ionization chamber, these particles travel from the wall of the chamber, which has a density similar to graphite, to a region that contains air, which presents a density around a thousand times lower. The energy loss along the CH step, the cross section calculation, the applied multiple scattering theory and the step size influence the particle transport in MC. Particle transport parameters must be as accurate as possible in order to avoid artefacts at the interface between regions of different density, when computing ionization chamber's response. MC algorithms and the transport parameters should be evaluated and optimised through the Fano test [37]. This test is supported by the Fano theorem which states that under conditions of Charged Particle Equilibrium (CPE), the charged particle fluence is independent of density variations from point to point considering that the cross-sections are uniform across the simulated phantom [38]. CPE exists for a certain volume V if each charged particle of a given type leaving the volume V is replaced by an identical particle of the same energy entering [16]. One way to implement this is to simulate an uniform particle distribution per unit mass and simulate the ionization chamber geometry with same molecular composition but varying densities. The density assigned to each region should correspond to its real density.

The Fano test was first applied to test particle transport algorithms for electrons. The first prerequisite to meet Fano's condition is to achieve CPE artificially throughout the geometry of the detector, as it is impossible to create this condition physically. There are two ways to implement the Fano test which were originally intended to test electron transport. One method, known as the regeneration technique, is based on a photon beam which sets in motion secondary electrons, creating CPE. As a photon beam traverses a medium, it will interact with matter according to the interaction cross sections and create secondary electrons. These are then followed throughout their tracks, and the photons are restored to their initial energy and momentum. Restoring the photons to their original state after they interact removes the possibility of having attenuated and scattered photons in the simulation. The photon beam is exclusively used to

generate electrons uniformly distributed in the medium so that CPE can be achieved. MC codes such as EGSnrc [39], PENELOPE [40] and Geant4 [41, 42] were validated for electron transport using this approach. The other alternative to implement the Fano test was introduced by Sempau and Andreo [43]. In their work, CPE was achieved by generating uniformly distributed electrons per unit mass throughout the simulated geometry. Since the interaction cross sections and the number of electrons per unit mass, I_e, are constant across the phantom, the absorbed dose in the medium, D, is the same in each region and it is simply calculated according to:

$$D = I_e \cdot E_i \tag{4.1}$$

where E_i is the the initial energy of all particles. Although both methods create the CPE condition, the latter is more direct and it is independent of photon cross sections. The MC code would pass the Fano test if the statistical uncertainties of the dose calculated in each region varied within 0.1%.

Only a few works in the literature have tested the MC transport algorithms for protons. The first study was carried out by Sterpin *et al* [44]. In their work, they have designed a hybrid Fano test based on both regeneration technique and the method introduced by Sempau and Andreo [43]. Analogous to the regeneration technique, which uses photon beams to create electrons, virtual particles undergoing an artificial interaction are created to produce protons. Upon these interactions, the virtual particles transfer all their energy to protons, and are then restored. Protons are set in motion with the same initial energy of the virtual particle that generated them and charged particle equilibrium is achieved. In this work, nuclear interactions were discarded as well as secondary electrons. The transport parameters were evaluated for the PENH (PENELOPE extended to protons) and Geant4 MC codes using this hybrid technique. Both MC codes passed the Fano test within 0.1%. Later, Wulff *et al.* have validated the proton transport in TOPAS/Geant4 [45]. Lourenço *et al.* [3] optimised the particle transport of protons and heavy charged secondary particles (including nuclear interactions) in FLUKA by generating a homogeneous proton source, as described by Sempau and Andreo. The Fano cavity test performed in this work is based on the developments of Lourenço *et al.* [3].

4.3 IONIZATION CHAMBER PERTURBATION CORRECTION FACTORS

Beam quality correction factors, k_{Q,Q_0}, have been calculated and published by the IAEA TRS-398 [12] for a large number of ionization chamber types used for reference dosimetry. For plane-parallel-plate ionization chambers, it was estimated that the relative standard uncertainty for k_{Q,Q_Q} in proton beams is 4.2% (k=2), leading to an uncertainty on the determination of absorbed dose-to-water for proton beams of the order of 4.6% (k=2). It is crucial to highlight that, according to the ICRU Report 24 [8], dosimetry uncertainties should be as small as possible, of around 1%, in order to have an overall uncertainty of 5% in the absorbed dose to the tumour. This means that an accurate calculation of k_{Q,Q_0} is essential in the determination of absorbed dose-to-water for proton beams as it is the main source of uncertainty [12]. Beam quality correction factors calculated in the IAEA TRS-398 [12] assume ionization chamber perturbation factors, p_Q, to be unity for all chambers tabulated independently of their chamber type. However, previous work have shown that these factors can amount to a correction of up to 1% for high-energy proton beams [15]. To reduce the uncertainty on k_{Q,Q_Q} factors, it is essential to determine accurately ionization chamber perturbation factors. Perturbation factors of ionization chambers have been extensively calculated, published in Codes of Practice and used in clinical practice for high-energy photon [46–48] and electron [43, 49–52] beams but, in contrast, perturbation factors for protons are still being established and not much research has been done in this field.

Gomà *et al.* [53] calculated beam quality correction factors, k_{Q,Q_0}, in proton beams for a set of ionization chamber models, according to the following formulation:

$$k_{Q,Q_0} = \frac{f_Q}{f_{Q_0}} \frac{W_{\mathrm{air},Q}}{W_{\mathrm{air},Q_0}} = \frac{(D_{\mathrm{water}}/D_{\mathrm{air}})_Q}{(D_{\mathrm{water}}/D_{\mathrm{air}})_{Q_0}} \frac{W_{\mathrm{air},Q}}{W_{\mathrm{air},Q_0}} \tag{4.2}$$

where W_{air} is the mean energy required to create an ion pair in air, D_{water} is the absorbed dose-to-water in the absence

of the ionization chamber and D_{air} is the absorbed dose-to-air in the cavity of the chamber, at the beam qualities Q (proton beam) and Q_0 (Cobalt-60 beam). The factor f is calculated as the product of the water-to-air stopping power ratio, $s_{\mathrm{water,air}}$, and the ionization chamber perturbation factor, p. Thus, an estimate of ionization chamber perturbation factors in the beam quality Q, p_Q, can be obtained through the ration of f_Q by $s_{\mathrm{water,air},Q}$.

Lourenço *et al.* [3] calculated ionization chamber perturbation correction factors for proton beams by considering different geometries of a plane-parallel-plate ionization chamber, as it is demonstrated in figure 4.2. D_{water} represents the dose in water in the absence of the chamber, D_{cavity} is the dose in the air cavity of the chamber in the absence of the rest of the geometry and D_{chamber} corresponds to dose in the air cavity when the full geometry of the chamber is taken into account. The perturbation factors due to the presence of the air cavity, p_{cav}, and the wall, p_{wall}, can be obtained through the dose ratios from one step to another. In their work, secondary electrons were discarded and the Bragg-Gray stopping power ratio was used in the calculations.

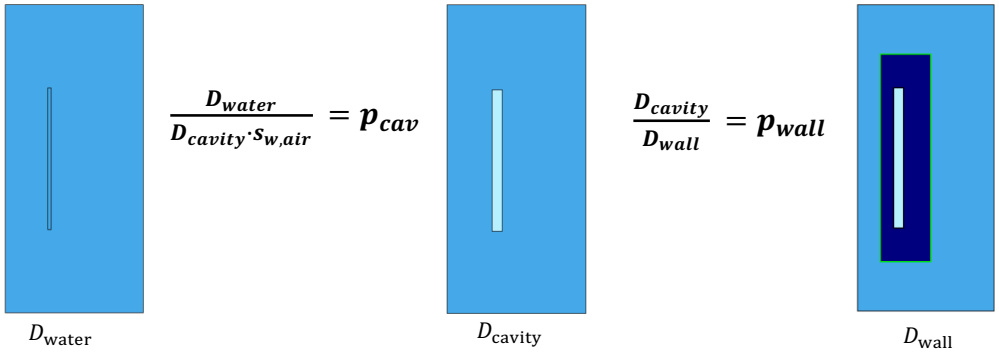

Figure 4.2: Illustration of the chain technique for the calculation of ionization chamber perturbation factors implemented by Lourenço *et al.* [3]

5 MATERIALS AND METHODS

5.1 FLUKA MONTE CARLO CODE

FLUKA MC code was used in the development of the present work. FLUKA is a multi-particle transport code developed by the Italian National Institute of Nuclear Physics (INFN) and European Organization for Nuclear Research (CERN) Collaboration Agreement. This code is a tool that allows one to calculate particle transport and interactions with matter for a broad number of applications, such as radiotherapy, dosimetry, detector design, as well as cosmic rays and neutrino physics. The FLUKA package includes physical models of interactions and propagation in matter for around 60 particle types, including photons, electrons, neutrons and heavy charged particles. Simple geometries can be combined to design complex regions for different simulation purposes. This combination is based on the Principle of Combinatorial Geometry and it is done by the boolean operations union, intersection and subtraction [54]. Rigorous and modern physical models are implemented and constantly updated in the FLUKA code by the FLUKA collaboration team. The input file of FLUKA consists of a sequence of commands, commonly called "cards", to specify the simulation options. There are around 80 cards with different functionalities available to the user to build their input file. Some cards are necessary to implement a complete and meaningful input file, such as those that define the radiation source, the geometrical set up, the corresponding materials of the geometry, the parameters for particle transport and the results to be scored. Other cards can be used to overwrite any default options [23, 24].

The detectors studied in this work are the PTW-34070 Bragg peak® and PTW-34001 Roos® chambers. The former has a sensitive volume with a radius of 4.08 cm and a thickness of 0.2 cm [55]; clinically, this chamber is used for range and percent depth-dose measurements. The PTW-34001 Roos® chamber is used for reference dose measurements and its sensitive volume has a radius of 0.78 cm and a thickness of 0.2 cm [56]. Both detectors are waterproof and their geometries were built in FLUKA according to the blueprints provided by the manufacturer.

The present work can be divided into two different sections. The first part consisted of the implementation of the Fano cavity test for a plane-parallel ionization chamber in order to validate the particle transport in the FLUKA Monte Carlo code for low-energy protons (20 MeV), when secondary charged particles are considered (including secondary electrons). The particle transport for protons with energies from 60 MeV to 250 MeV was validated previously by Lourenço *et al.* [57]. It is important to also validate the particle transport for lower-energies in order to study the chamber's response in the SOBP. In the second part, perturbation factors for the PTW-34070 Bragg peak® chamber in mono-energetic mono-directional beams were calculated where the full charged particle spectra was considered, including electrons. Computation of perturbation factors with the transport of all charged particles was also performed for the PTW-34001 Roos chamber in a SOBP. All simulations for both parts were performed in FLUKA version 2011.2x.3 [23, 24]. All data was analysed using MATLAB version R2018a.

5.2 THE FANO TEST

The Fano test was implemented based on the conditions of Fano's theorem. This test requires a specific design for the phantom, which must have the same atomic properties in all its regions but varying mass densities, and an uniform proton source per unit of mass has to be simulated.

5.2.1 PHANTOM GEOMETRY AND PROTON SOURCE

The PTW-Roos®chamber was simulated in a water phantom. The geometries were built in FLUKA using cylindrical and box shaped bodies defined by the RCC (Right Circular Cylinder) and RPP (Rectangular Parallelepiped) cards. The geometry of the ionization chamber was simplified and consisted of only two regions which were the air cavity and chamber's wall, which in the original geometry of the chamber is made of graphite. The outer shell of the chamber has a thickness of 1.04 cm and a diameter of 4.40 cm. The air cavity has a thickness of 0.20 cm and sensitive radius of

0.78 cm. The chamber was placed in the phantom region with dimensions of $26 \times 26 \times 6.8$ cm^3. All regions of the phantom were assigned the same material composition, so that the atomic properties were homogeneous across the whole geometry, but had different mass densities. The air cavity, chamber's wall and water phantom were assigned water-property materials but their original densities of 0.0012 g·cm^{-3}, 1.7 g·cm^{-3} and 0.998 g·cm^{-3}, respectively, were kept. For all three materials, the Sternheimer density effect parameters were added with the STERNHEI card and the I-value was set to 78 eV in the MAT-PROP card, according to the updated value for water in ICRU Report 90 [58]. The mass densities were overwritten using the MATERIAL card. The three regions built to implement the Fano test are represented in figure 5.1.

The second part of implementing the Fano test consisted of the generation of the source. The proton source must be homogeneous so that the number of particles per unit mass is uniform. To achieve this, the FLUKA "source.f" routine, which allows the implementation of non-standard particle sources, was modified. A plane-parallel source of 20 MeV protons was simulated and the number of particles generated in each region of the phantom was weighted by the correspondent density.

In the geometry simulated, one can distinguish two different regions: the build-up region and the CPE region. Conditions of CPE were not achieved at $z = 0$ in the phantom as particles were not generated before this point. The ionization chamber was placed within the CPE region where the dose should be uniform if the correct transport parameters were used in the physics list. If inconsistencies were found between the dose scored in the different mass density regions, then the transport parameters needed to be tuned. In this way, particle transport parameters could be optimised to be used in simulations to determine accurately the chamber's response. The whole set up for this test is shown in figure 5.1.

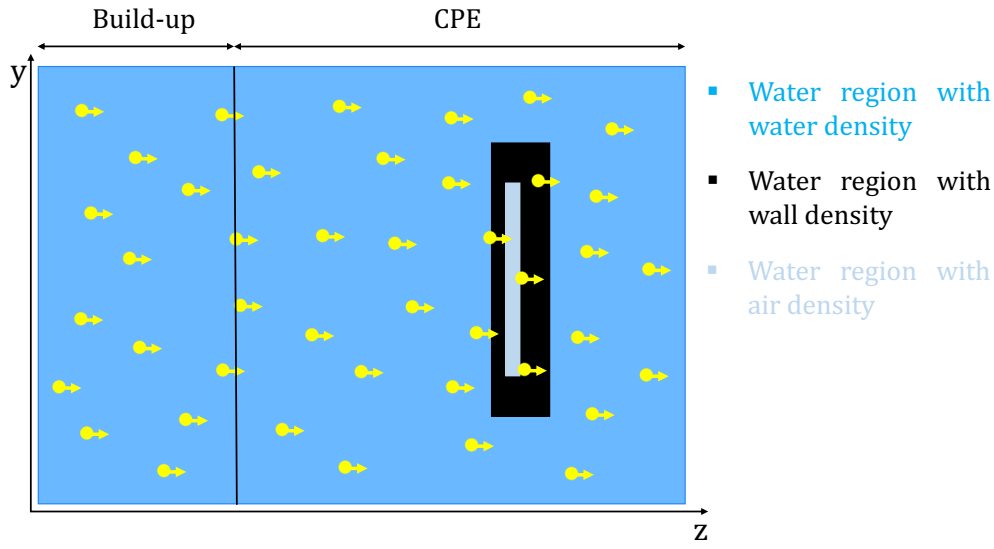

Figure 5.1: Schematics of the set up used for the Fano test. All regions of the phantom have water-property materials and it is divided into the buid-up and CPE regions. The light blue region has air density and it represents the cavity of the ionization chamber; the black region is the chamber's wall and it was assigned the density of graphite; the blue region represents the water region. The proton sources are represented by the yellow circles.

For each of the three regions with different densities, dose per primary was scored in a bin with the same dimensions as the air cavity using the USRBIN card. It was expected to obtain an uniform particle fluence per unit mass, $\Phi/\rho = constant$, as a homogenous proton source per unit of mass was simulated. According to the following equation,

$$D = \frac{\Phi}{\rho} \cdot S \tag{5.1}$$

if the fluence per unit of mass is constant, the dose, D, will be uniform across the phantom, as mass stopping powers are the same across the geometry. The materials in the different regions had the same atomic composition and the density effect in the stopping power formula was also made the same in all regions with different densities by overwriting in the STERNHEI card of each region the Sternheimer density effect parameters to be equal to that of liquid water.

5.2.2 PARTICLE TRANSPORT PHYSICS AND SCORING

The objective of this work was to study the accuracy of low-energy protons and secondary charged particle transport. The physics for particle transport was defined through the following cards:

- The DEFAULTS card determines the default options in FLUKA according to the problem. In this case, HADROTHErapy card was used to set the default options for hadron transport;
- The IONTRANS card, which determines the transport of ions, was set to full transport of all ions;
- The MULSOPT card was used for multiple Coulomb scattering optimisation;
- The PART-THR card defines the energy transport cut-off for hadrons. For protons, the transport cut-off was set to 10 keV. For heavier charged particles, the transport cut-off was set to 100 keV by default;
- The DELTARAY card was used to activate δ-ray production by charged hadrons. The threshold for production was set to 1 keV;
- The EMFFIX card was used to set the maximum fraction of the total energy that electrons could lose in a step to 0.1%;
- The STEPSIZE card was applied to control the maximum step size of all charged particles transported. The step size was set to 0.01 cm in order to minimize the boundary crossing artefacts.

The transport of all charged particles in a simulation was a very time-consuming process. To achieve a type A statistical uncertainty of 0.1% in the dose ratio, it was necessary to simulate one thousand independent runs of 10^7 primary protons. These simulations were performed in the UCL Myriad High Performance Computing Facility (Myriad@UCL) and they took around 26 000 CPU hours.

5.3 IONIZATION CHAMBER PERTURBATION CORRECTION FACTORS

Ionization chamber perturbation factors for the PTW-34070 Bragg peak® chamber and for the PTW-34001 Roos® chamber were calculated in narrow mono-energetic proton beams and in a broad modulated proton beam, respectively, using the approach presented by Lourenco *et al.* [3], considering the transport of all charged particles, including secondary electrons. In this section, the simulation procedures will be explained in detail.

5.3.1 IONIZATION CHAMBER PERTURBATION FACTORS IN NARROW MONO-ENERGETIC PROTON BEAMS

The full geometry of the PTW-34070 Bragg peak® chamber, represented in figure 5.2 (a), was modelled in FLUKA according to the blueprints. The regions were assigned the corresponding material, according to the manufacturer's specifications. Due to confidential agreements, only a simplified schematic of the chamber is shown in figure 5.2 (b) using the information available in the manufacturer's catalog [55]. The light blue region represents the air cavity of the chamber which has a thickness of 0.2 cm and a sensitive radius of 4.08 cm. The black region is the chamber's wall, mostly made of PMMA. The entrance window of this detector is made of a layer of PMMA, graphite and varnish, with thicknesses of 0.335 cm, 0.002 cm and 0.01 cm, respectively.

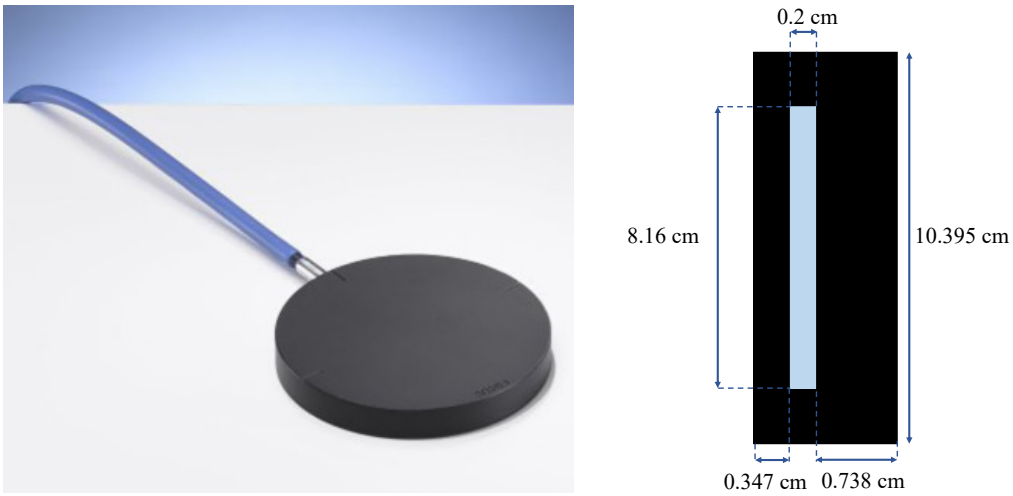

Figure 5.2: Representation of the PTW-Bragg Peak ionization chamber in sub-figure (a). Simplified schematics of the detector in (b). The light blue region represent the air cavity with a thickness of 0.2 cm and radius of 4.08 cm. The black region is the chamber's wall. The entrance wall has a total thickness of 0.347 cm.

As demonstrated in section 3.2.2, when using an ionization chamber for dose calculations, dose-to-water, D_{water}, is related to dose-to-air in the ion chamber, D_{chamber}, through the stopping power ratio between water and air, $s_{\text{water,air}}$, and the perturbation correction factor, p_Q. The perturbation correction factor accounts for the perturbation in the charged particle fluence due to the non-water equivalence of the different components of the chamber. In this work, the perturbation caused by the air cavity, p_{cav}, and the chamber's wall, p_{wall}, were evaluated, hence the dose-to-water can be expressed as follows:

$$D_{\text{water}} = D_{\text{chamber}} \cdot s_{\text{water,air}} \cdot p_{\text{cav}} \cdot p_{\text{wall}} \tag{5.2}$$

To calculate the perturbation introduced by the air cavity and the chamber's wall using MC, different geometries were considered as it is shown in figure 5.3. The first step, illustrated in sub-figure (a), consisted of calculating the dose in a thin layer of water, D_{water}. The thickness of the water layer, t_w, was set to 0.001 cm so that it has approximately a air cavity equivalent thickness. This layer was placed at a depth of $z_w - t_w/2$, where z_w is the depth of measurement in water. In the following step, sub-figure (b), dose-to-air, D_{air}, was scored in the air cavity at z_w. From these two steps, it was possible to infer the perturbation introduced by the presence of the air cavity, p_{cav}:

$$p_{\text{cav}} = \frac{D_{\text{water}}}{D_{\text{air}} \cdot s_{\text{water,air}}} \tag{5.3}$$

Finally, as shown in sub-figure (c), dose was determined in the air cavity of the chamber when simulating its full geometry, D_{chamber}. The front face of the ionization chamber was placed at a depth of z_w-WET, with WET being the water-equivalent thickness of the entrance window of the chamber. By comparing D_{air} and D_{chamber}, one can determine the perturbation introduced due to the presence of the chamber's wall, p_{wall}:

$$p_{\text{wall}} = \frac{D_{\text{air}}}{D_{\text{chamber}}} \tag{5.4}$$

The overall perturbation is given by the product of p_{cav} and p_{wall} as follows:

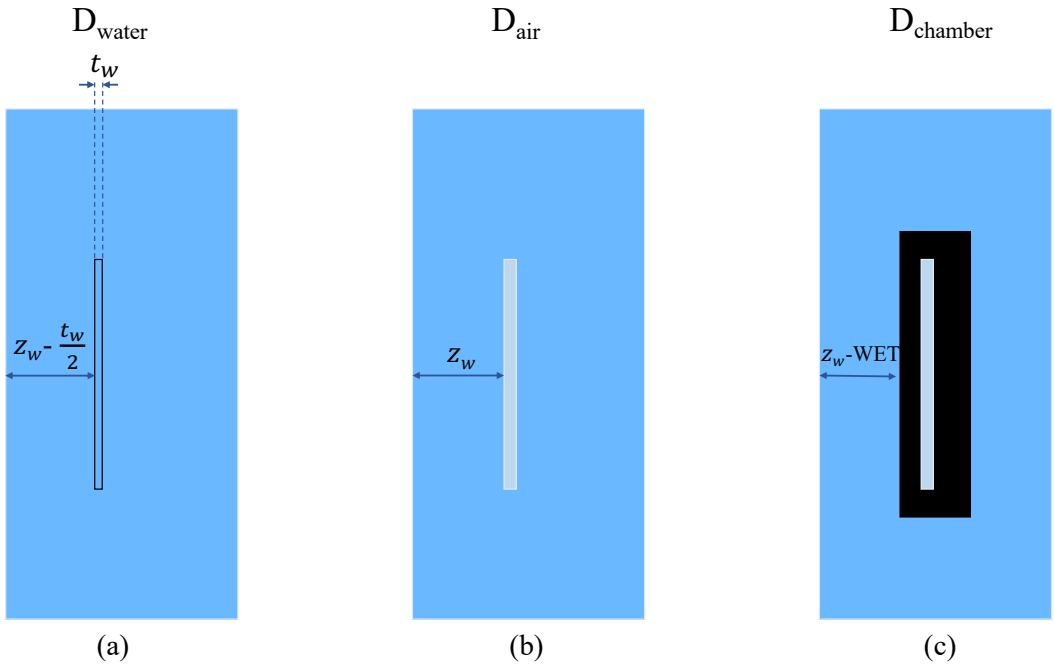

Figure 5.3: Simulation set up for the computation of ionization chamber perturbation correction factors. Water volume used to score dose-to-water, D_{water} in (a); simulated geometry to determine the dose deposited in the air cavity, D_{air} in (b); (c) geometry used to score the dose in the air cavity of the ionization chamber when its full geometry is considered, D_{chamber} in (c). t_w is the thickness of the layer of water simulated in (a), z_w is the depth of measurement and WET is the water-equivalent thickness of the entrance wall of the chamber.

$$p_Q = \frac{D_{\text{water}}}{D_{\text{chamber}} \cdot s_{\text{water,air}}} \tag{5.5}$$

The three geometries represented in figure 5.3 were placed in a box-shaped water phantom of $20 \times 20 \times 6$ cm^3. Perturbation corrections factors were calculated for mono-energetic mono-directional proton beams of 60 MeV, 150 MeV and 250 MeV. For the lowest energy of 60 MeV, a depth of measurement of $z_w = 1$ cm was chosen whereas for the 150 MeV and 250 MeV beams a depth of measurement of $z_w = 2$ cm was used.

5.3.1.1 The influence of secondary charged particles transport and physics settings

The influence of different charged particle types on p_Q was studied by simulating three different particle transport subsets for each beam energy.

i) All charged particles transported

In these simulations, primary protons as well as secondary charged particles produced from proton interactions with matter such as secondary protons, alphas, helions, deuterons, tritons and also electrons were considered. The transport of the full charged spectra represents the novelty of this work, as previous simulations only considered the transport of a set of particles [3, 53]. The physics for particle transport was the same as established to pass the Fano test [3]. D_{water}, D_{air} and D_{chamber} were scored using the USRBIN card. In order to calculate the perturbation correction factors, considering the production of secondary electrons, the Spencer-Attix mass stopping power ratio between water and air, $s^{\text{SA}}_{\text{water,air}}$, was used, as formulated by Spencer and Attix with Nahum track-ends [59]. When multiple charged particles contribute to the total absorbed dose in the medium, this quantity is calculated as follows [60]:

$$s^{\mathrm{SA}}_{\mathrm{water,air}} = \frac{\sum_i \int_{E^i_{\mathrm{cut}}}^{E_{\max}} \Phi^i_{\mathrm{water}}(E)(L_\Delta(E)/\rho)^i_{\mathrm{water}} dE + \Phi^i_{\mathrm{water}}(E^i_{\mathrm{cut}})(S(E^i_{\mathrm{cut}})/\rho)^i_{\mathrm{water}} E^i_{\mathrm{cut}}}{\sum_i \int_{E^i_{\mathrm{cut}}}^{E_{\max}} \Phi^i_{\mathrm{water}}(E)(L_\Delta(E)/\rho)^i_{\mathrm{air}} dE + \Phi^i_{\mathrm{water}}(E^i_{\mathrm{cut}})(S(E^i_{\mathrm{cut}})/\rho)^i_{\mathrm{air}} E^i_{\mathrm{cut}}} \tag{5.6}$$

where i represents the type of the charged particle in the beam, $E_{\max}$ is the maximum kinetic energy of the particle, $\Phi^i_{\mathrm{water}}(E)$ is the fluence differential in energy in the thin layer of water, $(L_\Delta/\rho)^i$ and $(S/\rho)^i$ are the mass restricted and unrestricted stopping powers, respectively, of the particle type i in the medium (water or air) and Δ is the $\delta-$ray production threshold. The transport energy cut-off, E_{cut}, for protons was set to 10 keV and for the remaining heavy charged particles, it was set to 100 keV. For electrons, $E_{\mathrm{cut}} = \Delta$ and it was set to 1 keV. The Spencer-Attix mass stopping power ratio was calculated offline from the fluence distribution and the stopping powers used in the simulations. The fluence was scored using the USRTRACK card for all charged particles. For heavy charged particles, both restricted and unrestricted mass total stopping powers used by FLUKA were printed by setting the option PRINT in the DELTARAY card. For electrons, it was only possible to print the restricted mass collision stopping power by using the option PRINT in the EMFCUT card. The unrestricted mass total stopping power was calculated separately, as explained below.

The unrestricted stopping power is the average rate of energy loss per unit path length. Thus, for electrons, this quantity was obtained by scoring the energy deposited by a single electron in a thin layer (10^{-5} cm) of water or air. The USRBIN card with the region binning option was used for this purpose. A script was written to generate electrons of different energies by substituting different energy values in the BEAM card. This method of obtaining the unrestricted stopping powers was first tested for protons, since the output file given by FLUKA prints the unrestricted stopping powers used by the code for hadrons. In both cases, the physics was established so that the energy loss by the particles was continuous where energy-loss fluctuations are neglected.

The transport parameters used to calculate the unrestricted stopping powers for protons in FLUKA were as follows:

- The DEFAULTS card was set to HADROTHErapy, which gives the default options for hadron transport;
- The DELTARAY card was used to switch off δ-ray production by setting the production threshold to infinity;
- The THRESHOL card was used to switch off elastic and inelastic nuclear interactions, by setting the threshold for these interactions to infinity;
- The IONFLUCT card was used to switch of ionization fluctuations.

For electrons, the following cards were used:

- The DEFAULTS card was set to PRECISIO, which gives the default options for precision simulations;
- The DELTARAY card was used to switch off δ-ray production;
- The THRESHOL card was used to switch off elastic and inelastic nuclear interactions;
- The IONFLUCT card was used to switch of ionization fluctuations;
- The EMFCUT card was used to set the energy thresholds for secondary electron and photon production.

To achieve a type A statistical uncertainty of 0.01% in the dose scored, it was necessary to simulate one thousand runs of 4×10^5 primary protons. The computation time to complete these simulation was of about 60 000 CPU hours.

ii) Electrons discarded

In this subset, the production of $\delta-$rays was switched off by setting the production threshold to infinity in the DELTARAY card. When secondary electrons are discarded, the Bragg-Gray mass stopping power ratio can be used to

calculate the perturbation corrections factors and it is derived as follows:

$$s^{\mathrm{BG}}_{\mathrm{water,air}} = \frac{\sum_i \int_0^{E_{\max}} \Phi^i_{\mathrm{water}}(E)(S(E)/\rho)^i_{\mathrm{water}} dE}{\sum_i \int_0^{E_{\max}} \Phi^i_{\mathrm{water}}(E)(S(E)/\rho)^i_{\mathrm{air}} dE} \tag{5.7}$$

where all quantities have the same meaning as described in equation 5.6.

iii) Nuclear interactions and electrons discarded

In these simulations, $\delta-$rays were discarded and elastic and inelastic nuclear interactions were switched off by choosing an infinite energy threshold for these interactions in the THRESHOL card. Protons were the only type of charged particles transported and the stopping power ratio was calculated by means of the Bragg-Gray formulation presented in equation 5.7.

The simulations performed for the subsets described in $ii)$ and $iii)$ were less computationally time-consuming. For each set-up, one thousand runs of 10^6 protons were simulated and only 1000 CPU hours were required.

5.3.2 IONIZATION CHAMBER PERTURBATION FACTORS IN A BROAD MODULATED BEAM

To compute ionization chamber perturbation factors in a SOBP, the full geometry of the PTW-34001 Roos® chamber, shown in figure 5.4 (a), was modelled in FLUKA, as described in section 5.3.1. The simplified schematic of this detector is shown in figure 5.4 (b), where the light blue region corresponds to the air cavity, which has a thickness of 0.2 cm and a sensitive radius of 0.78 cm. The black region represents the wall of the chamber, which is mostly made of PMMA. The entrance window of the chamber has a layer of PMMA, graphite and varnish, with thicknesses of 0.101 cm, 0.002 cm and 0.01 cm, respectively [56].

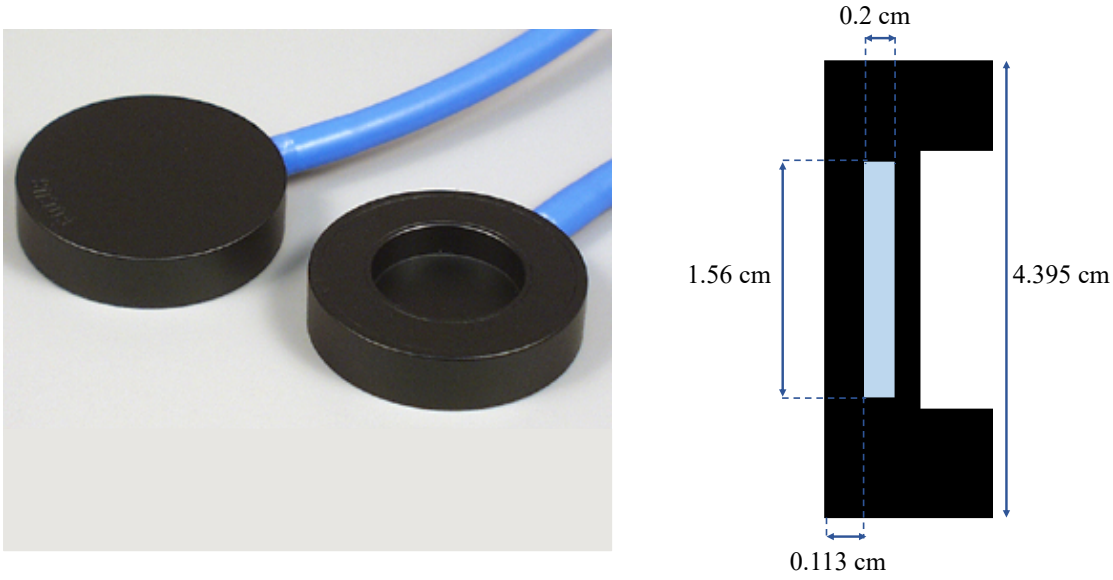

(a) (b)

Figure 5.4: Representation of the PTW-Roos® ionization chamber in (a). Simplified schematics of the detector in (b). The light blue region represents the air cavity with a thickness of 0.2 cm and radius of 0.78 cm. The black region is the chamber's wall. The entrance wall has a thickness of 0.113 cm.

A SOBP was implemented through a weighted superposition of mono-energetic proton beams (beamlets). In this

simulation, a $10 \times 10 \times 10$ cm^3 homogeneous dose field centred 15 cm deep in water was simulated. The reference depth, z_w, was in the middle of the SOBP, $z_w = 15$ cm. To meet the specifications of the SOBP, mono-energetic beams with energies from 117 MeV to 174 MeV, which have ranges of approximately 10 cm to 20 cm, respectively, were simulated. In order to obtain a region of high dose uniformity at the SOBP, each beamlet was assigned a specific weight, which was calculated by a MATLAB tool developed previously. As in the implementation of the source used in the Fano test (section 5.2.1), the FLUKA "source.f" routine was modified. The energies of the beamlets and their correspondent cumulative weights were introduced in this routine and the number of protons of each energy created was weighted according to their cumulative weights.

The same three geometries shown in figure 5.3 were simulated in a box-shaped water phantom of $20 \times 20 \times 30$ cm^3 to calculate D_{water}, D_{air} and D_{chamber}. In this case, the depth of measurement, z_w, was set to 15 cm, so that the scoring of dose was centred in the uniform dose region of the SOBP. In these simulations, ionization chamber perturbation factors were calculated for a single particle transport subset in which all secondary charged particles were transported. The same procedures as described in section 5.3.1.1 i) were followed.

One thousand runs of 5×10^5 primary protons were simulated to obtain a statistical uncertainty of 0.095% in the dose scored in each simulated geometry and the time to complete these simulations was of about 60 000 CPU hours. To reduce the uncertainties in the calculation of pQ factors, ideally, an uncertainty of around 0.01% should be achieved.

All simulations for mono-energetic beams with different particle transports and for the SOBP were performed using the UCL Myriad High Performing Computing Facility (Myriad@UCL) and the UCL Legion High Performing Computing Facility (Legion@UCL).

5.3.3 DETERMINATION OF THE WATER EQUIVALENT THICKNESS OF THE ENTRANCE WALL

The water equivalent thickness of the entrance window of the ionization chamber was calculated through MC simulations for each energy and transport subset, both for pencil beams and for the SOBP. To calculate the WET, two different geometries were simulated. One geometry consisted of the entrance wall of the chamber followed by a box shaped water region. An example of the set up of the simulation is shown in figure 5.5 (a). The second geometry simply consisted of the box shaped water phantom, shown in figure 5.5 (b). The $x \times y$ dimensions of the water region in blue were set to 20×20 cm^2. The z dimension was adjusted according to the range of the protons in the beam. The black dashed curves are typical examples of depth-dose deposition curves obtained in these simulation. The WET of the chamber wall was calculated by taking the difference between the range at 80% of the maximum dose, $R_{80\%}$, of the beam in the purely water phantom and that of the chamber wall plus water region. $R_{80\%}$ is the most appropriate range definition in mono-energetic beams as it corresponds to the range at which 50% of the protons have stopped.

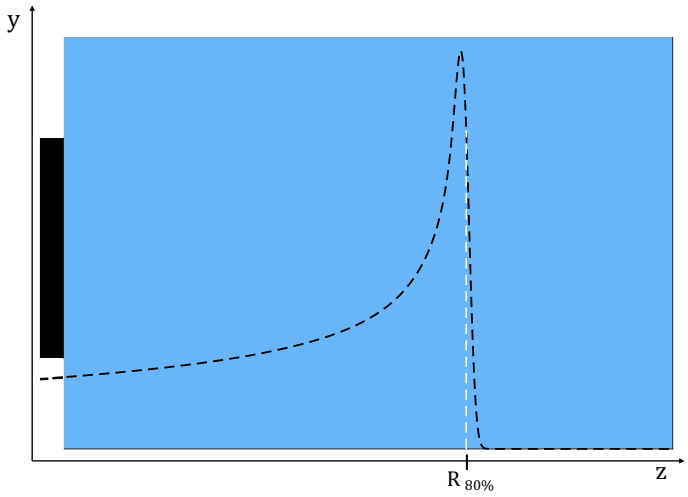

(a)

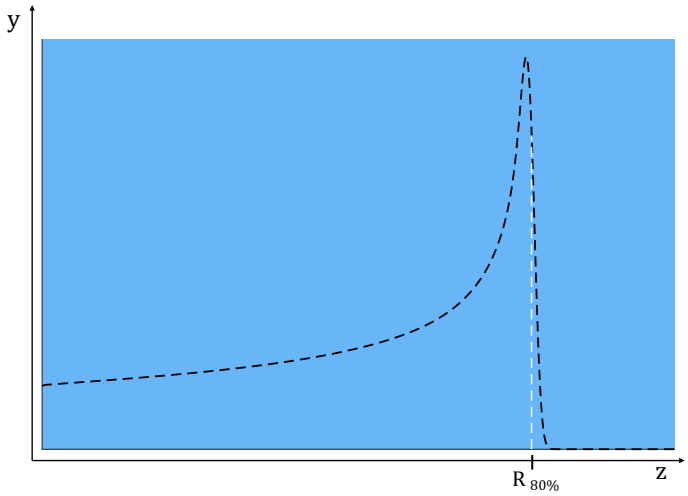

(b)

Figure 5.5: Simulation set up used for the calculation of the WET. The geometry of the entrance wall of the correspondent ionization chamber followed by a water region is show in (a) and the water phantom is shown in (b).

6 RESULTS AND DISCUSSION

6.1 THE FANO CAVITY TEST

Figure 6.1 shows the normalised depth-dose curve along the central axis of the water-property regions of the phantom used in the simulation. The dashed lines represent the position of the ionization chamber's regions in the phantom. The dose build-up region was small, less than half of a centimetre, since the range of 20 MeV protons in water is about 0.43 cm. Due to the scale of the plot, the dose looks like to be exactly the same in the whole CPE region although very small variations were found. Figure 6.2 represents the depth-dose curve along the central axis of the CPE region of the phantom, where fluctuations in the dose values were less than 0.1%.

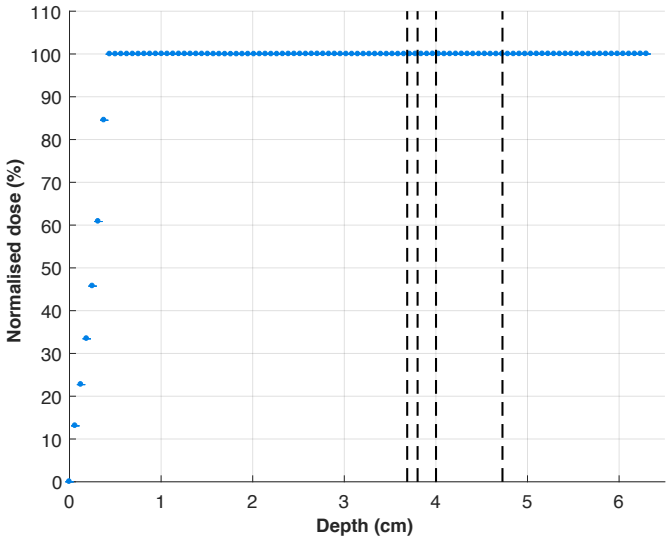

Figure 6.1: Depth-dose distribution of the homogeneous mono-directional plane-parallel proton source of 20 MeV simulated.

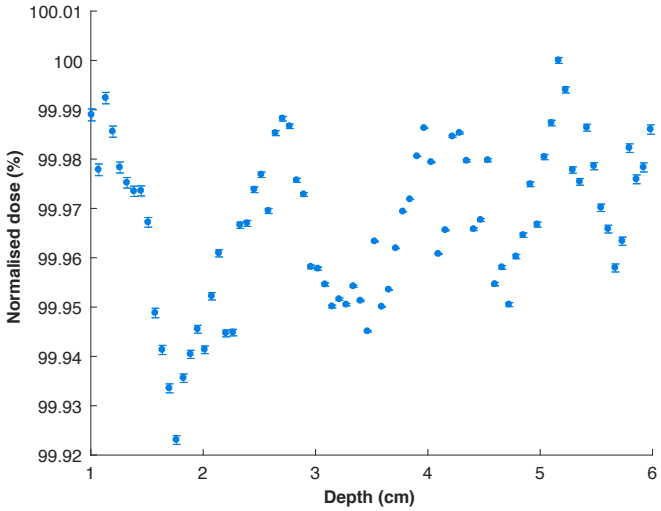

Figure 6.2: Depth-dose distribution in the CPE region of the homogeneous mono-directional plane-parallel proton source of 20 MeV simulated.

The dose values scored in each of the water-property regions are given in table 6.1. The statistical uncertainties (type A uncertainties) in the scored dose were found to be up to 0.06%.

Table 6.1: Dose values scored in the regions of the geometry simulated with different densities. The represented uncertainties are of type A.

$D_{\rho_{water}}$	$(6.956 \pm 0.004) \times 10^{-13}$ Gy/primary
$D_{\rho_{wall}}$	$(6.955 \pm 0.004) \times 10^{-13}$ Gy/primary
$D_{\rho_{air}}$	$(6.951 \pm 0.006) \times 10^{-13}$ Gy/primary

The dose ratios between different regions presented deviations of about 0.05% from unity. FLUKA passed the Fano cavity test within 0.1% accuracy when all particles were transported for a 20 MeV proton source. Lourenço *et al.* [57] validated the accuracy of FLUKA MC code for the energy range between 60 MeV and 250 MeV. The result for lower energies presented in this work is important to compute the response of an ionization chamber in the spread-out Bragg peak, where the dose is composed by pristine Bragg peaks of different initial energies.

A 2-dimensional representation of the dose across the water-property phantom is shown in figure 6.3 where dose is uniform in the CPE region.

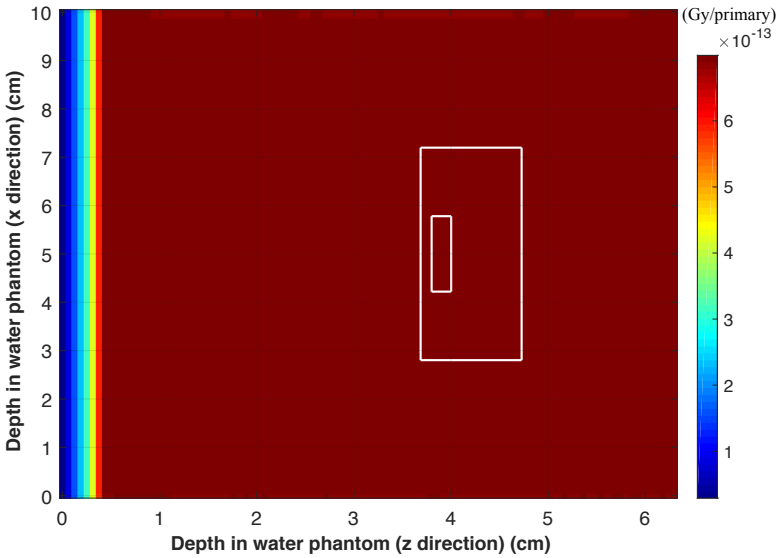

Figure 6.3: Dose distribution along the x and z axis of the water-property phantom.

6.2 IONIZATION CHAMBER PERTURBATION CORRECTIONS FACTORS

6.2.1 WATER-TO-AIR STOPPING POWER RATIOS

For the computation of perturbation factors, it was necessary to calculate the water-to-air mass stopping power ratios. The following results are related to the calculation of this quantity.

Figure 6.4 shows an example of the restricted and unrestricted stopping powers for protons in water used by FLUKA and printed in the output file. The curves started diverging at a energy of 0.459 MeV which was consistent with the chosen threshold of 1 keV for $\delta-$ray production. This result can be confirmed by the formula of the maximum energy transferred in a collision. When a particle with mass M transfers an energy E_{transf} to a free electron of mass m, the minimum energy that the projectile must have (E) is calculated as [2]:

$$E = \frac{1}{4} \cdot \frac{(M+m)^2}{M \cdot m} \cdot E_{\mathrm{transf}} \tag{6.1}$$

where $M = 1.673 \times 10^{-27}$ kg, $m = 9.109 \times 10^{-31}$ kg and $E_{\mathrm{transf}} = 1$ keV, which is the maximum energy transfer that can occur for an energy E of the incident particle. According to this formulation, the energy of the proton for which the restricted mass stopping power starts diverging from the unrestricted mass stopping power is 0.459 MeV. Consistent results were observed for the remaining charged particles in water as well as in air.

The unrestricted mass total stopping powers for electrons were calculated by scoring the energy deposited by a single particle in a thin layer of material. This approach was first tested for protons because FLUKA does not have the option to print the unrestricted stopping powers for electrons but it does for protons. The results showed a difference of 0.5% when compared to the unrestricted stopping power values used by FLUKA, printed in the output file. When the same results were compared to the values from NIST, a difference of 0.2% was observed. Note that, typically, published stopping powers for protons have uncertainties of up-to 4% at high energies and up to 15% at low energies (ICRU 1993). These results validated the approach implemented to calculate the stopping powers through simulation and thus the same approach was used to calculate the unrestricted stopping powers for electrons. The latter are plotted in figure 6.5. The blue curve represents the unrestricted mass total stopping power values for electrons in water from the NIST database. The orange points are the unrestricted stopping power values obtained by scoring the energy deposited by a single electron in a thin layer of water. The ratio of these results is shown in figure 6.6 and a maximum difference of about 0.7% was observed. Note that NIST stopping powers are provided for water with an $I-$value of 75 eV thus, for a consistent comparison, the same $I-$value was used in the simulations. However, an $I-$value of 78 eV was used for water in all simulations according to the recent ICRU Report 90; therefore, the stopping powers were re-calculated using the updated $I-$value. Similar findings were observed for air.

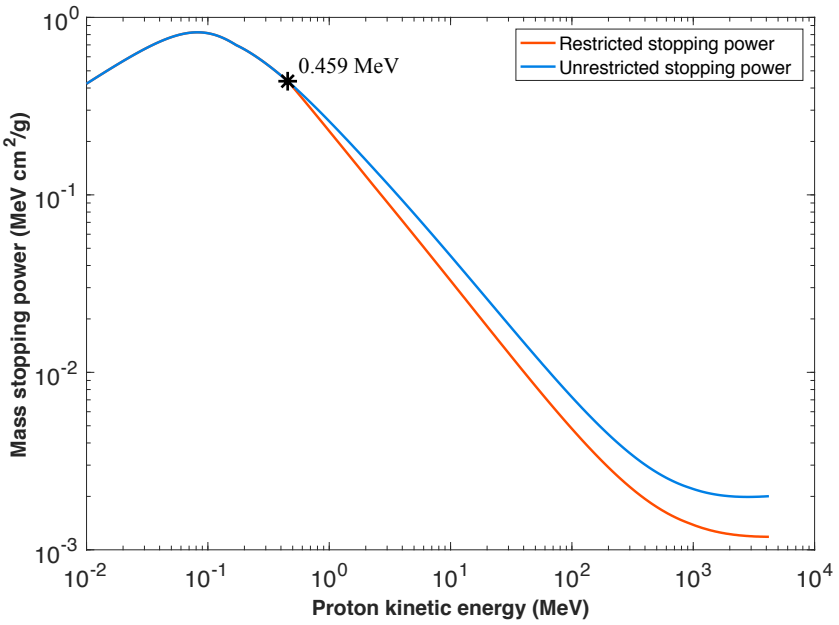

Figure 6.4: Restricted and unrestricted mass stopping powers in water for protons.

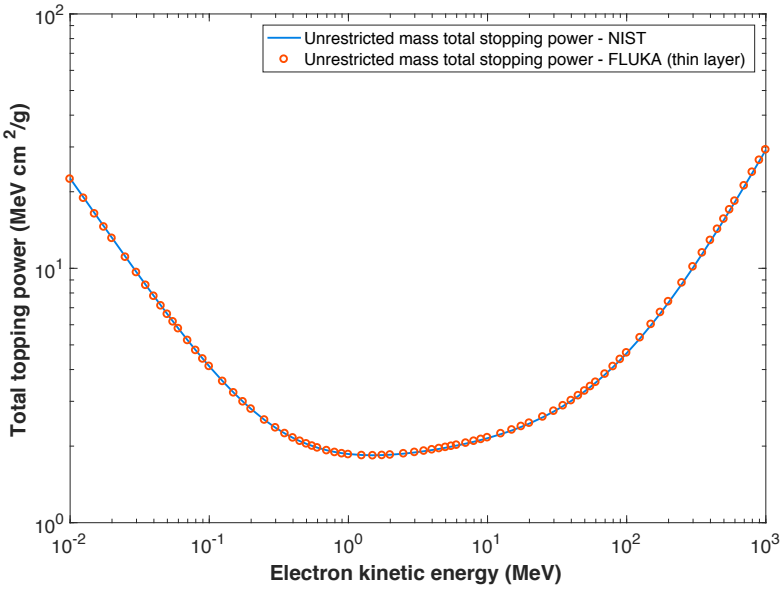

Figure 6.5: Comparison of the unrestricted mass total stopping power for electrons in water from NIST database and from the thin layer approach.

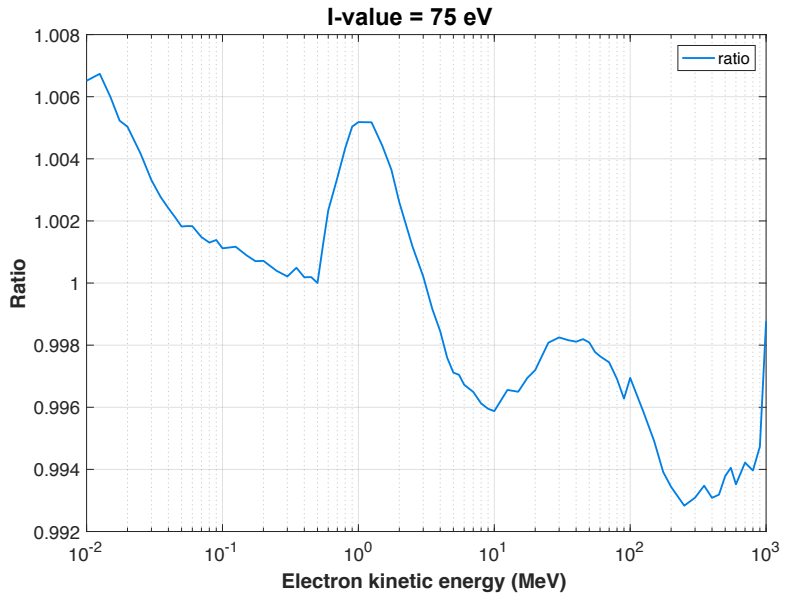

Figure 6.6: Ratio of the unrestricted mass total stopping powers obtained with FLUKA script to the unrestricted mass total stopping powers from NIST for electrons in water.

Finally, it was possible to calculate the proton stopping power ratios for each transport subset, for energies of 60 MeV, 150 MeV and 250 MeV and the results are shown in figure 6.7. The orange points represent the stopping power ratio for protons as nuclear interactions and electrons were discarded for this simulation. The points in blue are the stopping power ratios for all heavy charged particles. Both sets of results represent the Bragg-Gray stopping power ratio since none considered $\delta-$ray production. As one can see in figure 6.7, the difference between the two sets was minimal, less than 0.1%, which means that the influence of secondary heavy charged particles in the stopping power ratio is minor. The same conclusions were taken previously by Medin and Andreo [27] and Lourenço *et al* [3]. The black points correspond to the Spencer-Attix stopping power ratios since $\delta-$rays were considered. Medin and Andreo previously calculated the differences between the Bragg-Gray and Spencer-Attix stopping power ratios which amounted to 0.5%, when using PETRA MC code [27]. Differences of approximately 0.6% were found in this work which is comparable since different MC codes were used, as well as different transport cut-off energies. Gomà *et al* [61] calculated the water-to-air Spencer-Attix stopping power ratios and similar results were found. One of the objectives of their work was to study the effect of including electrons in the calculation of $s^{\mathrm{SA}}_{\mathrm{water,air}}$, when this quantity is calculated according to equation 5.6. They calculated $s^{\mathrm{SA}}_{\mathrm{water,air}}$ for protons alone and protons and electrons using the Spencer-Attix cavity integral in both situations. They found differences of only 0.1%, concluding that the effect of electrons could be considered negligible as long as the restricted stopping power, L_{Δ}, was used for protons. When all charged particles were included, differences in the $s^{\mathrm{SA}}_{\mathrm{water,air}}$ of around 0.2% were found between the results obtained in this work and the results of Gomà *et al*. Both BG and SA $s_{\mathrm{water,air}}$ showed to vary little with the initial energy of the beam - differences of approximately 0.25% were found when comparing the $s_{\mathrm{water,air}}$ at 60 MeV and 250 MeV.

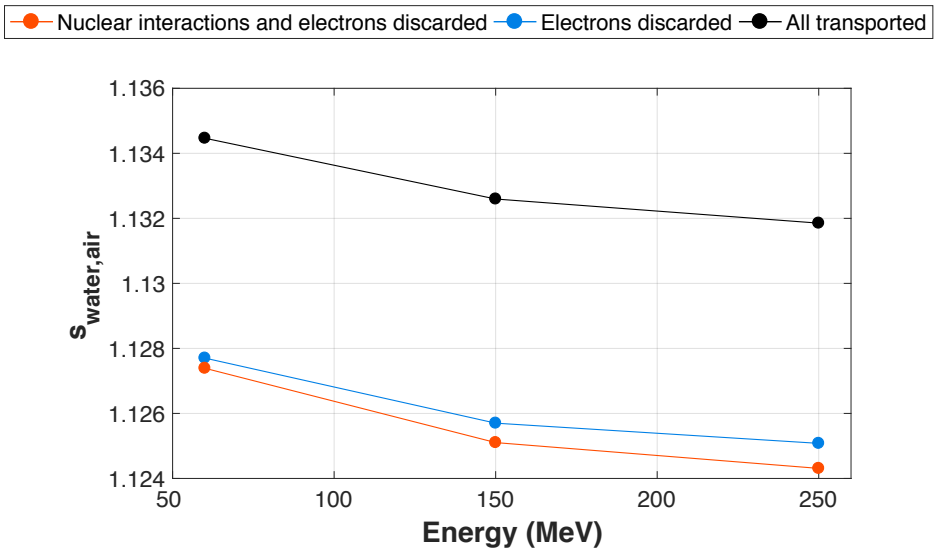

Figure 6.7: Bragg-Gray (orange and blue points) and Spencer-Attix (black points) water-to air stopping power ratios for proton beams of initial energies of 60 MeV, 150 MeV and 250 MeV when considering the transport of different particles.

6.2.2 WATER EQUIVALENT THICKNESS

Figure 6.8 below, shows an example of the calculations of the water equivalent thickness of the entrance wall of the PTW-34070 Bragg Peak® chamber for a 60 MeV beam when all charged particles were transported. The depth-dose distribution in blue considers the water phantom beyond the entrance wall of the detector while the orange curve is the depth-dose distribution in water without the entrance wall of the chamber. The difference in the range at 80% dose, R_{80}, between the two curves gives the WET of the entrance wall of the chamber which was approximately 0.39 cm with 5% uncertainty. The WET value was similar for all transport subsets considered at different proton initial energies and no particular trend was observed. The WET was calculated using the same procedure for the PTW-34001 Roos® chamber when a SOBP was simulated. The water-equivalent thickness of the entrance window for this detector was approximately 0.12 cm.

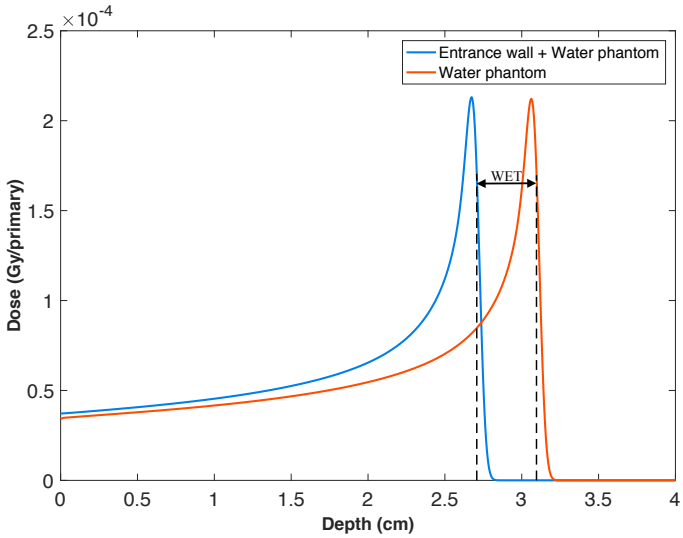

Figure 6.8: The curve in blue is the depth-dose distribution of a 60 MeV proton beam simulated in the entrance window of the PTW- Bragg Peak chamber followed by the water phantom. The orange curve represents the depth-dose distribution in the water phantom for the same beam. The water-equivalent thickness (WET) of the entrance window of the chamber is the difference between the range at 80% dose of the two curves.

6.2.3 PERTURBATION FACTORS IN NARROW MONO-ENERGETIC PROTON BEAMS

Figure 6.9 shows a 2-dimensional dose distribution for a 60 MeV proton beam for each geometry of the simulations considered (see figure 5.3) to compute the perturbation factors. In sub-figure 6.9 (a) the dose distribution is shown in the geometry with the presence of the thin layer of water in which dose was scored. No disturbance was observed in the dose. This suggests that the particle transport was optimised and no boundary artefacts were visible. Sub-figure 6.9 (b) represents the dose distribution in the water region with the presence of the air cavity. One can observe a disturbance in the dose distribution which occurred due to particle scattering when traversing a region made of water and a medium with lower density - in this case air. The same behaviour is observed in sub-figure 6.9 (c) when the full geometry of the chamber was considered. In this case, a slightly higher variation was observed in comparison with figure 6.9 (b).

Figure 6.10 represents the variation of the ionization chamber perturbation correction factors with energy for the different transport subsets considered in this work. As one can see in sub-figure 6.10 (a), p_{cav} was close to unity for all energies when different particles were transported, as verified by Lourenço *et al.* [3]. When nuclear interactions and electrons were discarded, p_{cav} was very close to unity. A maximum deviation from unity of only 0.3% was observed both when electrons were discarded and when all charged particles were considered. These values indicate that the perturbation introduced by the air cavity of the chamber in the charged particle fluence was not significant. Concerning the perturbation introduced by the chamber's wall represented in sub-figure 6.10 (b), when nuclear interactions and electrons were discarded, p_{wall} values were again approximately unity. In contrast, when secondary charged particles were considered, p_{wall} differed from unity: when electrons were discarded, a deviation of 0.3% and 0.9% was observed for the lowest and the highest energy, respectively; when all charged particles were transported, a deviation of 0.6% was observed for the 60 MeV proton beam and a deviation greater than 1% was observed for the 250 MeV beam. The increase in this perturbation factor with energy shows its energy dependence. The combined perturbation is shown in sub-figure 6.10 (c). Overall, similar results were found to those by Lourenço *et al.* [3], where perturbation factors did not differ much from unity, when nuclear interactions and electrons were discarded (orange points). This suggests that, when secondary charged particles are not transported, the approximation of the p_Q to unity is a good approximation, as it is suggested in the IAEA TRS-398 code of practice. However, deviations of up to 1% were also verified when

considering all secondary charged particles, as predicted by Palmans [15].

The calculated perturbation factors had a maximum statistical uncertainty of 0.05%.

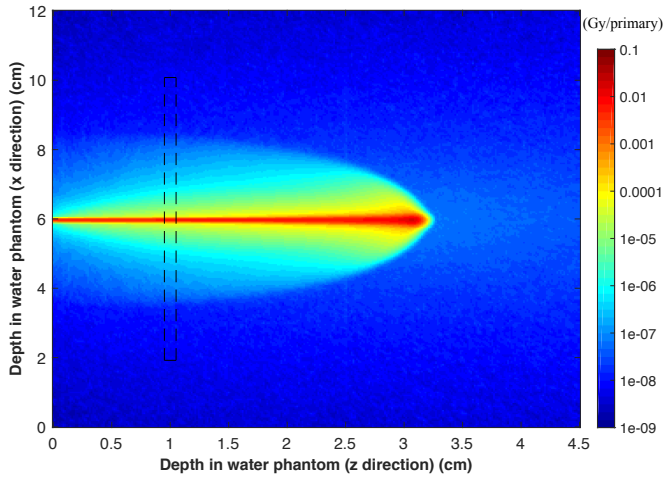

(a)

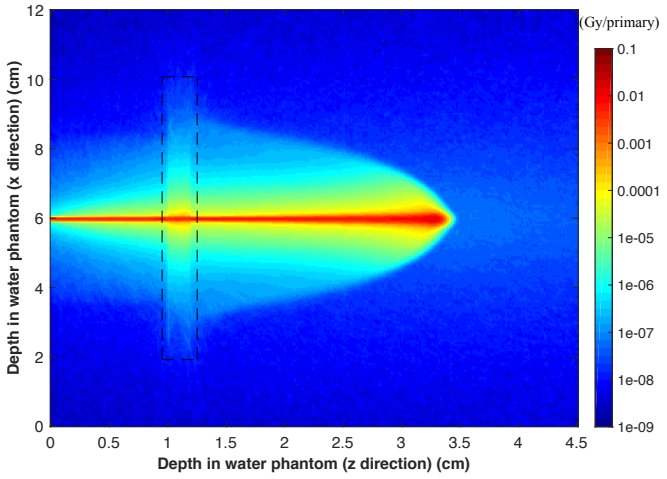

(b)

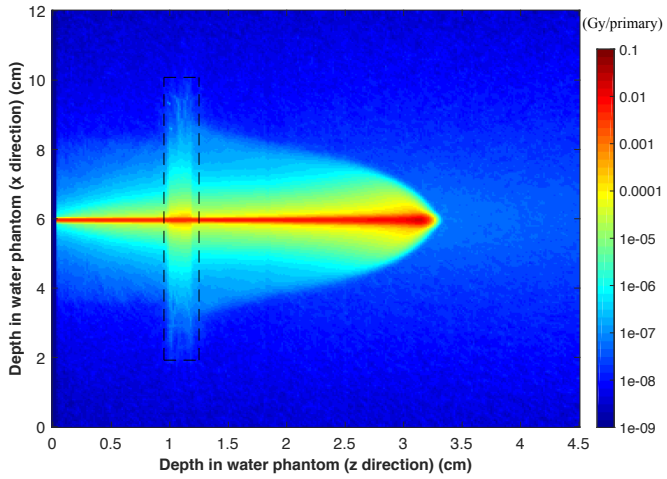

(c)

Figure 6.9: 2-dimensional dose distribution in the geometry used to score dose to water (a), in the geometry simulated to determine the dose in the air cavity (b) and in the geometry used to score the dose in the air cavity of the chamber when its full geometry is considered (c).

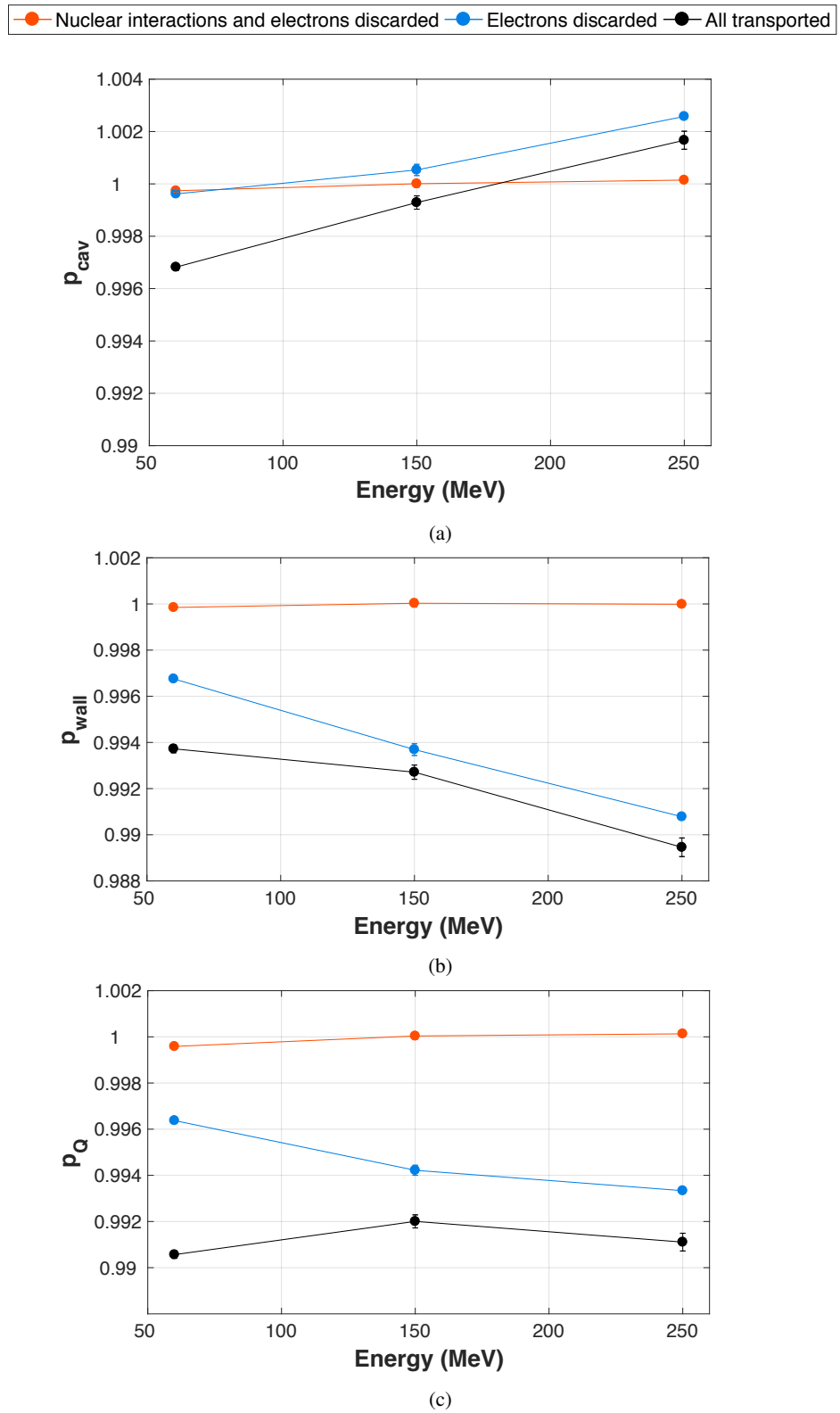

Figure 6.10: Ionization chamber perturbation correction factors as a function of the beam energy when all charged particles are transported (black points), electrons are discarded (blue points) and nuclear interactions and electrons are discarded (orange points). p_{cav} are represented in (a); p_{wall} are represented in (b) and the total perturbation, p_Q, is shown in (c).

6.2.4 PERTURBATION FACTORS IN A BROAD MODULATED BEAM

Figure 6.11 shows the normalised depth-dose curve along the central axis of a water phantom in which the SOBP was first tested. The build-up region of the SOBP was observed from 0 cm to 10 cm. The flat region, which corresponds to the uniform dose distribution region, can be seen from 10 cm to approximately 20 cm, followed by the distal fall-off region. The middle point of the flat region, z_w was at 15 cm. Figure 6.12 shows the normalised depth-dose curve along the central axis of the flat region of the SOBP. One can observe a maximum variation of 1.6% between the dose values within this region. Ideally, lower variations should be obtained, as well as lower uncertainties, in the dose values. In fact, a maximum variation of 0.1% was achieved with the algorithm built in MATLAB. To obtain a more uniformly distributed dose in the flat region of the SOBP through MC simulations, more histories need to be simulated.

Figure 6.13 shows a 2-dimensional dose distribution across the x and z axis of the water phantom. The non-uniformity of the flat region of the SOBP was also observed in the x axis.

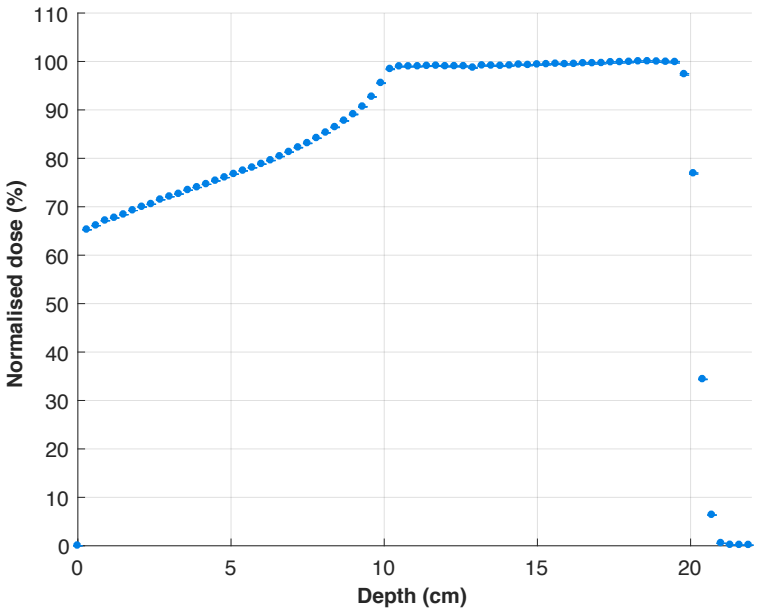

Figure 6.11: Depth-dose distribution of the SOBP simulated in the water phantom.

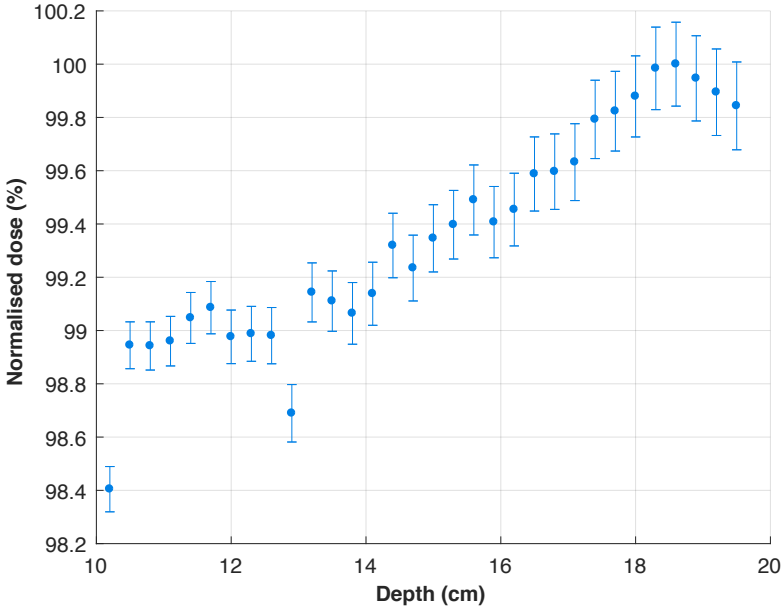

Figure 6.12: Depth-dose distribution of the flat region of the SOBP simulated in the water phantom.

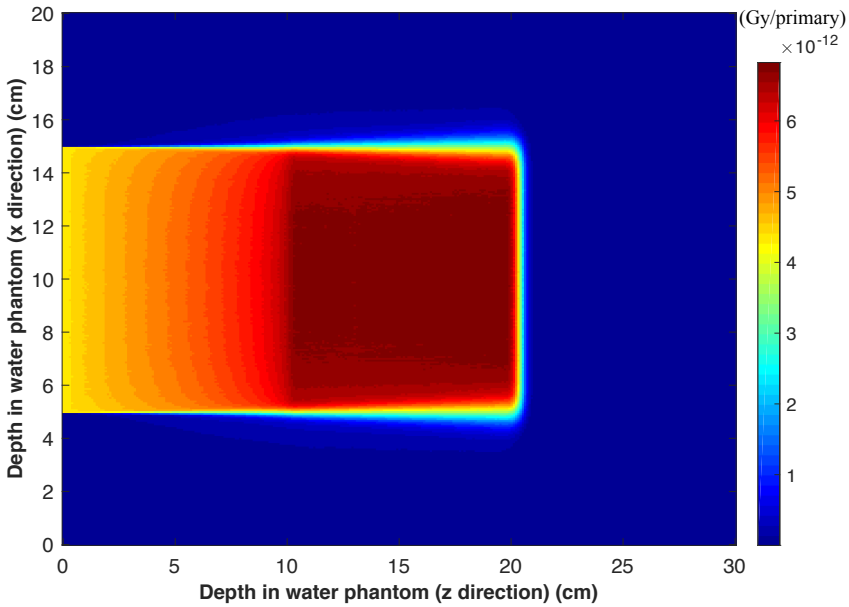

Figure 6.13: Dose distribution along the x and z axis in the water phantom simulated in a SOBP.

A variation of 1.6% in the uniform dose region of the modulated beam is too large in order to calculate significant ionization chamber perturbation factors, which are of the order of 1%. To achieve small statistical uncertainties, these simulation are in fact extremely time consuming and would take approximately 120 000 CPU hours. Due to limited resources, these results could not be obtained.

7 CONCLUSION

In this work, the particle transport in FLUKA MC code was validated for low-energy protons by performing a Fano cavity test. FLUKA passed the Fano cavity test within 0.1% accuracy for a plane-parallel ionization chamber when all secondary charged particles were transported, including electrons.

Ionization chamber perturbation factors were calculated for the PTW-34070 Bragg Peak® chamber in narrow mono-energetic proton beam and for the PTW-34001 Roos® chamber in a broad modulated beam. A necessary step in this work was the calculation of the water-to-air stopping power ratios, which showed low energy dependence. Differences of 0.6% between Bragg-Gray and Spencer-Attix water-to-air stopping power ratios were found. The results of the ionization chamber perturbation factors for mono-energetic proton beams showed that, when nuclear interactions and electrons were discarded, p_Q was close to unity for all energies considered. In contrast, when nuclear interactions were considered, p_Q differed from unity by around 0.7%. When all secondary charged particles were transported, perturbation corrections amounted to approximately 1%. The increase in the perturbation correction with the transport of both heavy charged particles and electrons suggests that secondary charged particles influence in fact this quantity, thus need to be considered to compute the chamber's response accurately.

To decrease the uncertainty in k_{Q,Q_0}, ionization chamber perturbation factors must be calculated accurately and include the transport of the full charged spectra to account for the non-water equivalence of the air cavity and wall of these detectors.

Simulations of ionization chamber perturbation factors in broad modulated proton beams showed to be extremely time consuming. Further investigations must consider the calculation of these factors in the SOBP.

REFERENCES

[1] Harald. Paganetti, editor. *Proton Therapy Physics, Series in Medical Physics and Biomedical Engineering*. Florida, crc edition, 2011.

[2] Pedro Andreo, David Burns, Alan Nahum, Jan Seuntjens, and Frank Herbert Attix. *Fundamentals of Ionizing Radiation Dosimetry*. Number June. WILEY-VCH, 2017.

[3] Ana Lourenço, Hugo Bouchard, Sebastian Galer, Gary Royle, and Hugo Palmans. The influence of nuclear interactions on ionization chamber perturbation factors in proton beams: FLUKA simulations supported by a Fano test. *Medical Physics*, 46(2):885–891, 2019.

[4] World Health Organization. Cancer key facts. *The Lancet Global Health*, 2018.

[5] J Ferlay, I Soejomataram, M Ervik, R Dikshit, S Eser, C Mathers, M Rebelo, DM Parkin, D Forman, and F Bray. World Cancer Research Fund International Worldwide Data, 2012.

[6] Michael Goitein. *Radiation Oncology: A Physicist's-Eye View*. Biological and Medical Physics, Biomedical Engineering. Springer New York, New York, NY, 2007.

[7] J. R. (Jerry R.) Williams and D. I. Thwaites. *Radiotherapy physics–in practice*. Oxford University Press, Oxford ;;New York, 2nd ed. edition, 2000.

[8] ICRU report 24. Determination of Absorbed Dose in a Patient Irradiated by Beams of X or Gamma Rays in Radiotherapy Procedures. *Journal of the International Commission on Radiation Units and Measurements*, os13(1):NP–NP, 1976.

[9] W C Roentgen. On a New Kind of Rays. *Nature*, 53(1369):274–276, 1896.

[10] Rajamanickam Baskar, Kuo Ann Lee, Richard Yeo, and Kheng-Wei Yeoh. Cancer and radiation therapy: current advances and future directions. *International journal of medical sciences*, 9(3):193–9, 2012.

[11] ICRU report 85: fundamental quantities and units for ionizing radiation. *International Commission on Radiation Units and Measurements*, 150(4):550–552, jul 2012.

[12] P Andreo, D Burns, K Hohlfeld, M Huq, Tatsuaki Kanai, F Laitano, V Smith, and Stanislav Vatnitsky. *Aborbed dose determination in external beam radiotherapy: an international code of practice for dosimetry based on standards of absorbed dose to water*. Vienna, iaea techn edition, 2000.

[13] K Hohlfeld. The Standard DIN 6800: Procedures for absorbed dose determination in radiology by the ionization method (IAEA-SM-298/31). In *Dosimetry in Radiotherapy. Proc. IAEA Symp. (Vienna 1987)*. Vienna.

[14] Joakim Medint, Pedro Andreot, Erik Orusell, Olle Mattssong, and Martin Roost. Physics in Medicine & Biology Related content Ionization chamber dosimetry of proton beams using cylindrical and plane parallel chambers . N w versus N K ion chamber calibrations Ionization chamber dosimetry of proton beams using cylindrical and plane par. 1995.

[15] Hugo Palmans and Stanislav Vatnitsky. Chapter: dosimetry and beam calibration. In WI: Medical Physics, editor, *Principle, Practice of Proton Beam Therapy (Medical Physics Monograph)*, pages 317–51. Madison, edition, 2015.

[16] Frank Herbert Attix. *Introduction to Radiological Physics and Radiation Dosimetry*. Wiley-VCH Verlag GmbH, Weinheim, Germany, nov 1986.

[17] M. J. Berger, M. Inokuti, H. H. Andersen, H. Bichsel, D. Powers, S . M. Seltzer, D . Thwaites, and D. E. Watt. Stopping Power and Ranges for Proton and Alpha particles-Report 49. *Journal of the International Commission on Radiation Units and Measurements*, os25(2):NP–NP, may 1993.

[18] M. J. Berger, M. Inokuti, H. H. Anderson, H. Bichsel, J. A. Dennis, D. Powers, S. M. Seltzer, and J. E. Turner. Report 37. *Journal of the International Commission on Radiation Units and Measurements*, os19(2):NP–NP, dec 1984.

[19] Ervin B. Podgorsak. *Radiation Physics for Medical Physicists*. Biological and Medical Physics, Biomedical Engineering. Springer Berlin Heidelberg, Berlin, Heidelberg, 2010.

[20] J. E. (James Edward) Turner. *Atoms, radiation, and radiation protection*. Wiley, 1995.

[21] William R. Leo. Passage of Radiation Through Matter. In *Techniques for Nuclear and Particle Physics Experiments*, pages 17–68. Springer Berlin Heidelberg, Berlin, Heidelberg, 1994.

[22] J. F. Ziegler. Stopping of energetic light ions in elemental matter. *Journal of Applied Physics*, 85(3):1249–1272, 1999.

[23] T. T. Böhlen, F. Cerutti, M. P.W. Chin, A. Fassò, A. Ferrari, P. G. Ortega, A. Mairani, P. R. Sala, G. Smirnov, and V. Vlachoudis. The FLUKA Code: Developments and challenges for high energy and medical applications. *Nuclear Data Sheets*, 120:211–214, 2014.

[24] A Ferrari, P R Sala, A Fassò, and J Ranft. FLUKA: A multi-particle transport code. (SLAC-R-773. CERN-2005-010. INFN-TC-2005-11), 2005.

[25] M B Chadwick, D T L Jones, H H Barschall, R S Caswell, P M Deluca, J-P Meulders, A Wambersie, H Schuhmacher, P G Young, L J Cox, G M Hale, U J Schrewe, and J V Siebers. Nuclear Data For Fast Neutron and Proton Therapy-Report 63. Technical report.

[26] Leena Al-Sulaiti. Fluence correction factor for various materials in clinical proton dosimetry. 2012.

[27] Joakim Medin and Pedro Andreo. Monte Carlo calculated stopping-power ratios, water/air, for clinical proton dosimetry (50 - 250 MeV). *Physics in Medicine and Biology*, 42(1):89–105, jan 1997.

[28] Christian P. Karger, Oliver Jäkel, Hugo Palmans, and Tatsuaki Kanai. Dosimetry for ion beam radiotherapy. *Physics in Medicine and Biology*, 55(21), 2010.

[29] Hugo Palmans, Frank Verhaegen, Jean Marc Denis, Stefaan Vynckier, and Hubert Thierens. Experimental pwall and pcel correction factors for ionization chambers in low-energy clinical proton beams. *Physics in Medicine and Biology*, 46(4):1187–1204, 2001.

[30] Seuntjens, J., Strydom, W., Shortt, K. Chapter 2: Dosimetric principles, Quantities and Units. In *Review of Oncology Physics: A Handbook for Teachers and Students*, number January 2005. International Atomic Energy Agency, Vienna, 2005.

[31] Paul Mobit and George Sandison. Cavity Theory. In Y. Horowitz, editor, *Microdosimetric Response of Physical and Biological Systems to Low-and High-LET Radiations*, chapter 5, pages 331–366. 2006.

[32] J. W. Boag and J. Currant. Current collection and ionic recombination in small cylindrical ionization chambers exposed to pulsed radiation. *The British Journal of Radiology*, 53(629):471–478, may 1980.

[33] Glenn F. Knoll. *Radiation detection and measurement*. John Wiley, 2010.

[34] Nicholas Metropolis and S Ulam. The Monte Carlo Method. *Journal of the American Statistical Association*, 44(247):335–341, sep 1949.

[35] Ernesto Amato, Domenico Lizio, and Sergio Baldari. Applications of the monte carlo method in medical physics. *Medical Physics*, (March 2013):105–113, 2013.

[36] P. Andreo. Monte Carlo techniques in medical radiation physics. *Physics in Medicine and Biology*, 36(7):861–920, 1991.

[37] Joao. Seco and Frank. Verhaegen. *Monte Carlo techniques in radiation therapy*. CRC/Taylor & Francis, 2013.

[38] U. Fano. Note on the Bragg-Gray Cavity Principle for Measuring Energy Dissipation. *Radiation Research*, 1(3):237, 1954.

[39] I. Kawrakow. Accurate condensed history Monte Carlo simulation of electron transport. II. Application to ion chamber response simulations. *Medical Physics*, 27(3):499–513, 2000.

[40] Josep Sempau, Pedro Andreo, Judith Aldana, Jocelyne Mazurier, and Francesc Salvat. Electron beam quality correction factors for plane-parallel ionization chambers: Monte Carlo calculations using the PENELOPE system. *Physics in Medicine and Biology*, 49(18):4427–4444, 2004.

[41] Emily Poon, Jan Seuntjens, and Frank Verhaegen. Consistency test of the electron transport algorithm in the GEANT4 Monte Carlo code. *Physics in Medicine and Biology*, 50(4):681–694, 2005.

[42] Cancer Research UK.

[43] J. Sempau and P. Andreo. Configuration of the electron transport algorithm of PENELOPE to simulate ion chambers. *Physics in Medicine and Biology*, 51(14):3533–3548, 2006.

[44] Edmond Sterpin, Jefferson Sorriaux, Kevin Souris, Stefaan Vynckier, and Hugo Bouchard. A Fano cavity test for Monte Carlo proton transport algorithms. *Medical Physics*, 41(1):011706, dec 2013.

[45] Jörg Wulff, Kilian Simon Baumann, Nico Verbeek, Christian Bäumer, Beate Timmermann, and Klemens Zink. TOPAS/Geant4 configuration for ionization chamber calculations in proton beams. *Physics in Medicine and Biology*, 63(11), 2018.

[46] P Andreo. Absorbed dose beam quality factors for the dosimetry of high-energy photon beams. *Physics in Medicine and Biology*, 37(12):2189, 1992.

[47] J. Wulff, K. Zink, and I. Kawrakow. Efficiency improvements for ion chamber calculations in high energy photon beams. *Medical Physics*, 35(4):1328–1336, 2008.

[48] J. Wulff, J. T. Heverhagen, and K. Zink. Monte-Carlo-based perturbation and beam quality correction factors for thimble ionization chambers in high-energy photon beams. *Physics in Medicine and Biology*, 53(11):2823–2836, 2008.

[49] M. Bailey, D. R. Shipley, and J. W. Manning. Roos and NACP-02 ion chamber perturbations and water-air stopping-power ratios for clinical electron beams for energies from 4 to 22 MeV. *Physics in Medicine and Biology*, 60(3):1087–1105, 2015.

[50] F. Verhaegen, R. Zakikhani, A. DuSautoy, H. Palmans, G. Bostock, D. Shipley, and J. Seuntjens. Perturbation correction factors for the NACP-02 plane-parallel ionization chamber in water in high-energy electron beams. *Physics in Medicine and Biology*, 51(5):1221–1235, 2006.

[51] Lesley A. Buckley and D. W.O. Rogers. Wall correction factors, Pwall, for parallel-plate ionization chambers. *Medical Physics*, 33(6):1788–1796, 2006.

[52] F. Araki. SU-GG-T-207: Monte Carlo Calculations of Correction Factors for Plane-Parallel Ionization Chambers in Clinical Electron Dosimetry. *Medical Physics*, 35(6):2773, 2008.

[53] Carles Gomà, Pedro Andreo, and Josep Sempau. Monte Carlo calculation of beam quality correction factors in proton beams using detailed simulation of ionization chambers. *Physics in Medicine and Biology*, 61(6):2389–2406, 2016.

[54] Margaret B. Emmett. MORSE: Present capabilities and future directions. In *Applied Radiation and Isotopes*, 2000.

[55] PTW. Bragg Peak Ionization Chambers. *https://www.ptwdosimetry.com/en/products/bragg-peak-ionization-chambers/*, 2019.

[56] PTW. Roos Electron Chamber. *https://www.ptwdosimetry.com/en/products/roos-electron-chamber/*, 2019.

[57] Ana Lourenço, David Shipley, Hugo Bouchard, Gary Royle, and Hugo Palmans. Evaluation of the Particle Transport Accuracy in the FLUKA Monte Carlo Code for Proton Therapy Dosimetry Applications. In *Proceedings of the 57 Annual Meeting of the Particle Therapy Cooperative Group (PTCOG). International Journal of Particle Therapy: Fall 2018, Vol. 5, No. 2*, pages pp. 58–229., 2018.

[58] ICRU report 90. Key Data for Ionizing-Radiation Dosimetry: Measurement Standards and Applications. *Journal of the International Commission on Radiation Units and Measurements*, 14(1):1–118, 2016.

[59] A. E. Nahum. Water/air mass stopping power ratios for megavoltage photon and electron beams. *Physics in Medicine and Biology*, 23(1):24–38, 1978.

[60] M. Laitano, F. and Rosetti. Proton stopping powers averaged over beam energy spectra. *Physics in Medicine and Biology*, 45:3025–45, 2000.

[61] C Gomà, P Andreo, and J Sempau. Spencer–Attix water/medium stopping-power ratios for the dosimetry of proton pencil beams. *Physics in Medicine and Biology*, 58(8):2509–2522, apr 2013.